2017

Single atom alloy catalysts for C-H bond activation and propane dehydrogenation

A thesis submitted by

Joshua Wimble

in partial fulfillment of the requirements for the degree of

Master of Science

in

Chemical Engineering

Tufts University

May 2017

Adviser: Maria Flytzani-Stephanopoulos

Abstract

Single atom alloys (SAAs) have shown considerable promise as heterogeneous catalysts for a wide range of industrially important reactions, by providing atomically dispersed active species to enable near 100% atom efficiency in catalytic systems. These materials are explored in this thesis for C-H bond activation reactions, which have become increasingly relevant in recent years as crude oil production in the US has become lighter due to increases in shale oil production. Single atom platinum, palladium, and nickel in the surfaces of supported copper nanoparticles were prepared by galvanic replacement for comparison to their monometallic nanoparticle counterparts in C-H bond activation reactions in butane and propane. As part of this work, deactivation kinetics were compared, for the first time, between single atom Pt, Pd, and Ni in Cu nanoparticles and their monometallic nanoparticle counterparts. The PtCu- and PdCu-SAAs were shown to have superior coke resistance when compared to Pt and Pd nanoparticles under realistic propane dehydrogenation conditions in a fixed bed reactor. For our reactions, we demonstrated that coke production rates are reduced by more than 90% in PdCu- and PtCu-SAAs. Deactivation mechanisms considered for PtCu- and PdCu-SAAs were most consistent with particle sintering and subsurface metal atom diffusion, while their monometallic equivalents were more consistent with deactivation by coking. Similar results were found for the C-H bond activation in butane, tested by H-D exchange over a range of temperatures. Additionally, reaction rates were measured for each system, and the apparent activation energies, E_{app}, were calculated. These measurements were performed approximately at steady-state, but on partially deactivated catalysts. The extent of deactivation due to carbon deposition was different among the three metals. The E_{app} were similar between single atom alloys and monometallic catalysts in contrast to DFT calculations performed elsewhere, showing that SAA catalysts should have higher E_{app} . E_{app} were as follows: for Pt and PtCu = 77±3 and 68±9 kJ/mol; for Pd and PdCu = 30±2 and 35±5 kJ/mol; and for NiCu-SAAs 17±5 kJ/mol. The reason for the different apparent activation energies between Pt and Pd is attributed to

pore closure by carbon deposition in the latter. Excessive coking and very low reaction rates made calculation of activation energies over monometallic Ni nanoparticles impractical for our system. This is the first time that ambient pressure catalytic measurements in propane dehydrogenation were made for this series of bimetallic single atom catalysts, allowing for comparison between expected DFT trends and actual experimental data. This type of work will allow rational catalyst design to further refine the understanding of materials needed to allow access to low cost fine chemicals produced from olefins.

Acknowledgements

I would like to thank Professor Maria Fiytzani-Stephanopoulos for her help and direction during the project despite my somewhat unorthodox schedule and Jilei Liu for his work on the C-H bond activation portion of this work and his help orienting me around the lab. Finally, a special thank you to my fiancé Amanda Colby without whom leading a normal life these last two years would have been impossible.

Contents

Single atom alloy catalysts for C-H bond activation and propane dehydrogenation

Chapter 1 – Introduction and Literature review

Ethylene and propylene are important commodity chemicals, both of which are starting materials for a wide range of industrially relevant compounds. Most of the world's supply of these compounds has traditionally been provided by steam cracking, utilizing many different feedstocks that vary based on region and proximity of crude oil reserves. In the steam cracking process, complex aromatic and alkane feedstocks are cracked into lighter target olefins, which are then separated for further use. Typical physical properties for heavy naphtha, one feedstock of interest in light alkene production, are listed below in Table 1.

Table 1 - Typical characteristics and composition of heavy naphtha (1)

Initial boiling point (°C)	149
Final boiling point (°C)	204
Paraffins (vol%)	46
Naphthenes (vol%)	42
Aromatics (vol%)	12

In particular, ethylene and propylene are produced in substantial quantities from this process, which supports growing demand for plastics and other commodity chemicals globally. Since the relative ratios of ethylene to propylene are typically fixed to a narrow range based on process conditions and feedstock composition, growing demand for polypropylene over polyethylene during the last 15 years has created an environment with significant strain on the propylene supply (1). Several of the industrially important materials produced from propylene are detailed in Figure 1.

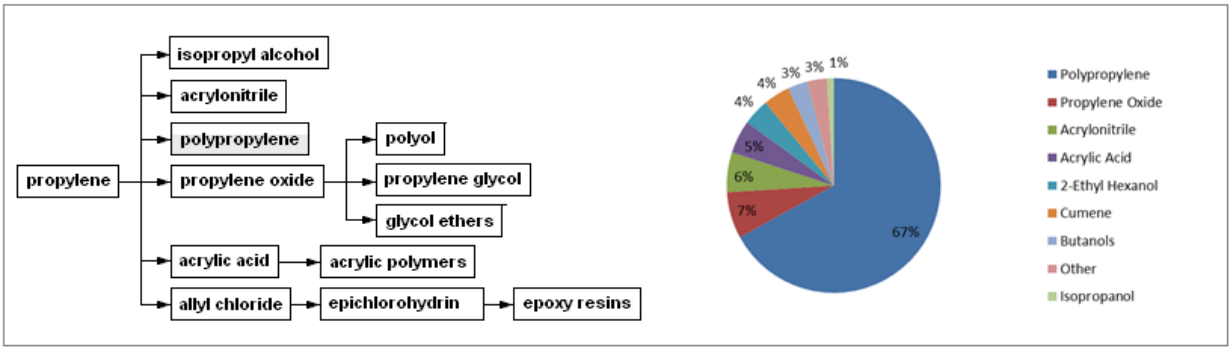

Figure 1 –Major chemicals made from propylene and global production in 2015 (1) (2)

In addition to the relative increase in propylene demand, shifting feedstock supplies have created pressure on the markets as well. Shale gas production in the US has increased dramatically due to both technological advances that allow access to previously infeasible reserves, as well as strategic decisions made by the Obama administration to improve the security of our energy economy (3). As the US usage of foreign crude oil for heating and chemical synthesis has declined, the available feedstock sources have adjusted accordingly. Table 2 below provides an overview of typical compositions for shale gas at the well-head. Shale gas is rich in light alkanes (C_1-C_4), and provides no large organics for cracking.

Table 2 - Typical shale gas composition in the US (4)

Component	Vol% at wellhead
Methane	70-90
Ethane	0-20
Propane	
Butane	
Pentane	<1
Hexane	<1
Nitrogen	0-5
Carbon Dioxide	0-8
Hydrogen Sulfide	0-5
Noble Gases	trace

Figure 2 below provides some insight into drastically increasing shale gas production due to the afore mentioned factors.

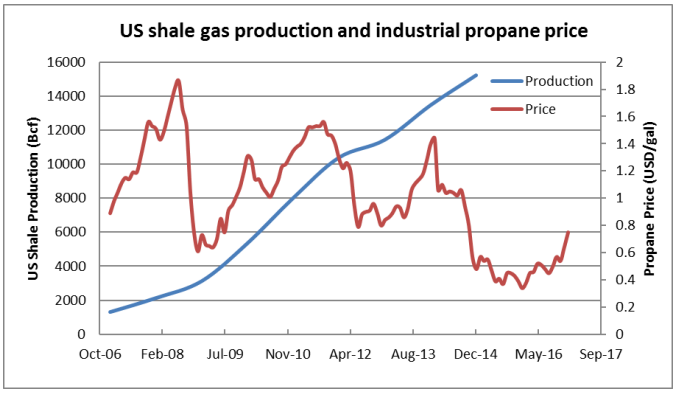

Figure 2 - Shale gas production in the United States (3) (4)

This shift in feedstocks to a lighter composition has created an abundance of light alkanes, driving down prices while at the same time providing very little propylene to the marketplace relative to the steam cracking and fluidized catalytic cracking (FCC) that it displaced. The difference in propylene production and demand has created a so-called “propylene gap”.

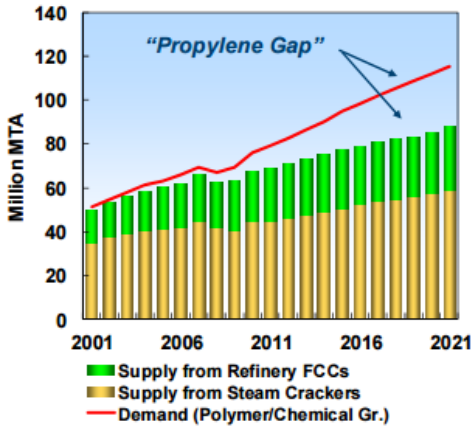

Figure 3 - Production gap for propylene from traditional sources (5)

The combination of these economic factors has led to the construction of several “on-purpose dehydrogenation” plants in the US, which take advantage of the cheap propane feedstock to directly produce propene in a catalytic process.

On demand PDH and state of the art

Universal Oil Products (UOP) Oleflex

One of the most widespread catalytic operations for propane dehydrogenation is the Oleflex system from UOP. This system uses an alumina supported platinum and tin catalyst to produce propene and hydrogen from propane, through a dehydrogenation process operated between 550-650^{o}C (6). To help overcome over-dehydrogenation, these units are typically operated with a liquid phase selective hydrogenation process to convert diolefins and other side products to propylene. Through process optimization and coupling to additional reactor trains, yield loss due to coking and subsequent dehydrogenation of monoalkenes are kept low to help improve economics. Additionally, this system uses UOP's patented continuous catalyst regeneration (CCR) process to constantly remove catalyst from the reactor and regenerate it in a separate system before reinjection to the dehydrogenation reactors. Details of the operating economics can be found elsewhere but since hydrocarbon byproducts can be used for their heating value, the expected return on investment for new plants is largely controlled by propane prices. The Oleflex process is currently the industry choice for propane dehydrogenation (PDH) technology, with 32 of the 37 dehydrogenation projects bid between 2011 and 2015 opting for this technology (7).

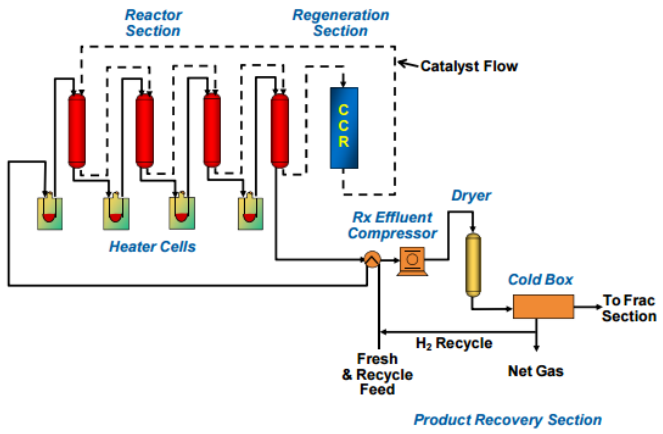

Figure 4 - PFD overview of the UOP PDH process (Oleflex) (5)

CB&I's Catofin Process

A direct competitor of UOP's Oleflex is the Catofin process from CB&I. As with these other processes, the Catofin process was originally a research and development effort driven by a need to produce butadiene from butane. This was driven by the increasing demand for more styrene-butadiene rubber and polybutadiene as a result of the post-World War II economic expansion (8) . In contrast to UOP's catalyst, CB&I uses a proprietary catalyst without noble metals (7). Instead, the dehydrogenation is accomplished by ~20% CrO_x supported on alumina with small amounts of Na and K (6). This process is operated under vacuum to lower the partial pressure of the reactants and further drive the equilibrium controlled reaction to products. Figure 5 below presents a typical process flowsheet.

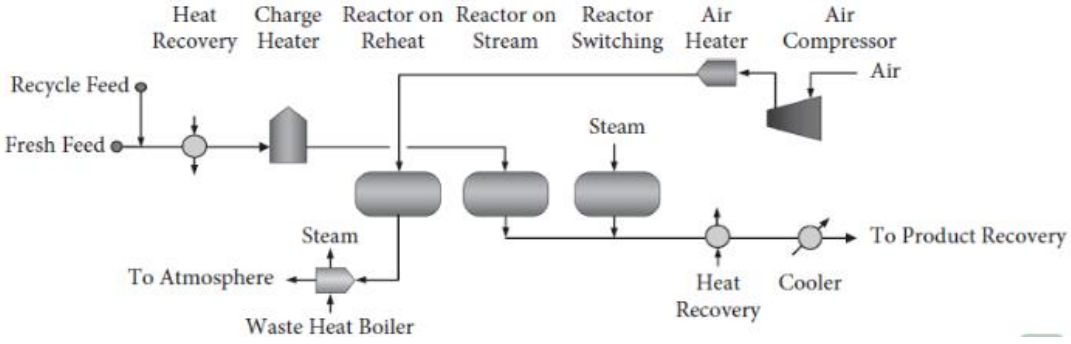

Figure 5 - Typical PFD for the Catofin process. Reprinted with permission from American Chemical Society (6)

In the Catofin process, several fixed bed reactors are operated in parallel. These beds undergo alternating regeneration/reduction/dehydrogenation cycles using air to burn off coke deposits and reheat the catalyst and hydrogen to reduce the catalyst. The reactors are operated adiabatically, and the regeneration cycles are also utilized to reheat the bed before returning the reactors to the dehydrogenation service. They are then operated until the bed temperature decreases enough that equilibrium conversions are low, and they are then regenerated. Typical cycle time is approximately 20 minutes (7).

Texas Petrochemicals (TPC)/UOP OXO-D Process

In addition to the previously detailed dehydrogenation processes, there are commercially viable oxidative dehydrogenation (ODH) processes available, though these are typically used for C_4 dehydrogenations. In contrast to the standard dehydrogenation reaction, ODH is unique in that the overall process it is exothermic. ODH eliminates some of the main drawbacks of standard PDH. The presence of oxygen avoids the requirement for occasional regeneration cycles and allows for much lower reaction temperatures (9), which leads to significantly reduced energy costs (7). Additionally, produced H_2 is oxidized to water eliminating the thermodynamic constraints of non-oxidative PDH. However, ODH is characterized by relatively low yields and poor selectivity which has prevented its adoption in commercial scale units.

Other routes to propylene

In addition to the dehydrogenation routes discussed above, there are also several other commercially viable processes for propylene production. Olefin metathesis or disproportionation reactions where ethylene and butenes are used to produce propylene in high yields with first generation catalysts based on tungsten or molybdenum are also in use. Methanol-to-olefin technology is used to convert syngas from natural gas or other sources to methanol then to light alkenes over acidic zeolites. Similarly,

fluidized catalytic crackers can be used to convert gas oil to propylene over zeolite catalysts (10). Further, chromium (III) oxide and several other metal oxide catalysts have shown effective for ODH and PDH at the lab scale (11) (12).

Technical basis for work

To understand the basis of rational catalyst design in PDH reactors, it is first important to discuss the origins of the catalytic activity of metals for dehydrogenation. The earliest commercial dehydrogenation processes used chromium oxide-based catalysts to convert readily available butane to butadiene for use in synthetic rubber, and 1-butene was dimerized to make octane for aviation fuels (6). Although these metal oxide catalysts exhibit many similarities in mechanism to noble metal catalysts, we mention them only briefly here to expand the mechanistic view of this reaction. The Catofin process discussed previously is an example of an industrially important reaction that uses chromia catalysts. However, in recent years, platinum-based catalysts have gained market share due to increased activity and slower deactivation rates.

Dehydrogenation catalysts and mechanistic view

Metal catalysts

Although platinum is the metal traditionally used for dehydrogenation catalysts, many other transition metals also show activity for this reaction. For the purposes of this research, we focused on platinum, palladium, and nickel, since each of these metals have shown activity for dehydrogenation reactions in the literature. To understand the role of transition metals in catalysis, it is illustrative to look at one of the proposed mechanisms for propane dehydrogenation over platinum metal. It is worth noting that there is still debate over the true mechanism, and that it may be different for each catalyst system (6) (13). The Horiuti-Polanyi mechanism shown in Figure 6 is commonly used to describe dehydrogenation over metal catalysts.

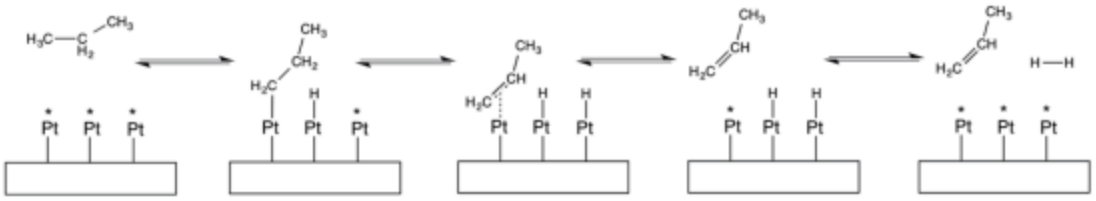

Figure 6 - Horiuti-Polanyi mechanism for dehydrogenation of propane. Reprinted with permission from American Chemical Society (6)

Briefly, the alkane undergoes dissociative adsorption on to the active site followed by cleavage of a second C-H bond to form either a π-bonded alkyl group (shown in Figure 6) or a di-σ-bonded group. Diffusion away from the active site by the associated hydrogen atoms, followed by formation of a hydrogen molecule and desorption of H_2 and propylene, complete the catalytic cycle. Following this mechanism, the role of platinum is to act as a Lewis acid and accept electrons from C-H σ bonds during the adsorption step. Nickel and palladium function in similar ways.

The electronic configuration and local environment of these metals is strongly influenced by support effects as well, and d-band theory has shown much success in describing the adsorption behavior of gas phase species on metallic surfaces. In the case of bimetallics, shifts in d-band energy levels can lead to stronger or weaker adsorbate binding relative to bulk metal. Sykes et al showed that with palladium-copper bimetallics, surface palladium atoms showed a d-band shift away from the Fermi level, which is expected to lead to weaker adsorbate binding, while on a gold surface, they reported the opposite (14). In a similar fashion, Jang et al demonstrated this sharp reduction in H_2 adsorption affinity for palladium doped copper (15).

There are a number of successful theories that provide the framework for the rational design of bimetallic catalysts. Perhaps the most well-known is the Sabatier principle, which qualitatively describes the relationship between adsorption strength and reaction rate. Visualizing this principle gives rise to the well-known volcano plots. Figure 7 below shows the variation of reaction rate with oxygen binding

energy on various metals for CO oxidation. Note the characteristic maximum when the binding energy is "just right" to promote high turnover frequencies.

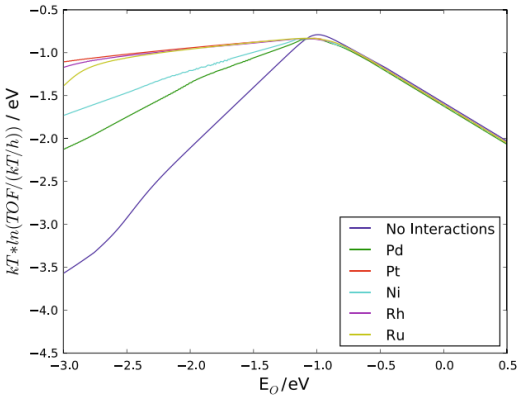

Figure 7 - Volcano plot showing reaction rate for CO oxidation as a function of oxygen binding energy on several metals. Used with permission from (16).

The available data provides a conceptual model for this type of behavior, where weak adsorption provides little surface adsorbed material for reaction, while strongly adsorbing systems prevent the desorption of product species blocking active sites. In each extreme, the reaction rate is retarded compared to intermediate adsorption strengths. A successful bimetallic catalyst should then be one that exploits the impact of the secondary metal on the adsorption properties of the highly active metals, such as Pt.

Metal oxide catalysts

The accepted mechanism for dehydrogenation reactions over metal oxides shows some similarity to that of noble metals. Presented below is one proposed mechanism taken from Sattler et al (6).

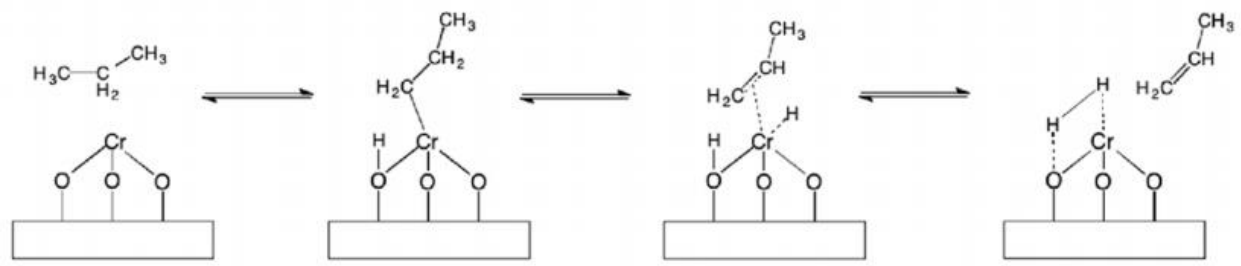

Figure 8 - Proposed mechanism for propane dehydrogenation over chromium oxide. Reprinted with permission from American Chemical Society (6)

Here, we see the first C-H bond cleavage during dissociative adsorption resulting in the creation of an adjacent hydroxyl group, and a σ-bond to the active site chromium atom. Further C-H bond scission forms a Cr-H bond and a π-bond, ending in a similar configuration to the platinum catalyst in Figure 6. Finally, elimination of a hydrogen molecule and desorption of propene recovers the catalyst for another cycle.

Rate laws and Rate-limiting steps

It is well established in the literature that the rate-limiting step in light alkane dehydrogenation is initial C-H bond activation and scission on the catalyst surface. This is demonstrated both experimentally through a comparison of Gibbs free energies (17), as well as computationally using density functional theory (DFT) calculations (6).

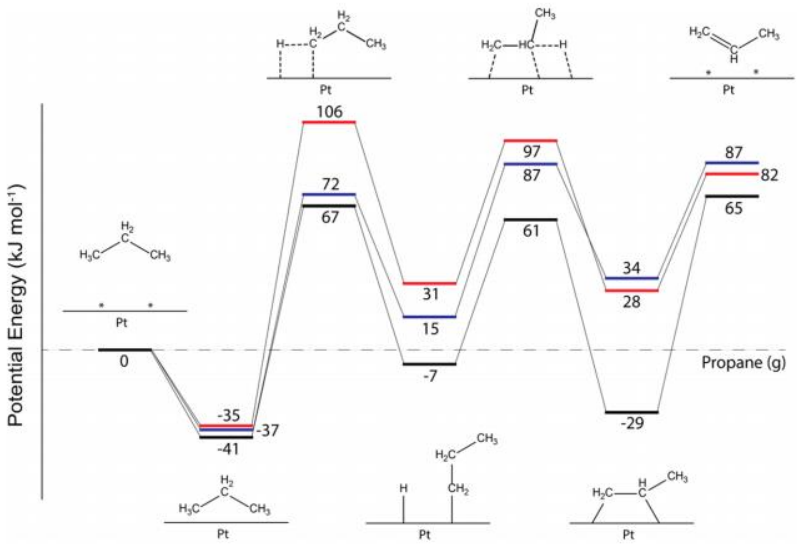

Figure 9 - Potential energy reaction coordinate for PDH over platinum and platinum tin alloys from DFT calculations on Pt(111) (black), Pt_3Sn(111) (blue) and Pt_2Sn(111) (red). Reprinted with permission from American Chemical Society (6)

Figure 9 maps out the potential energy landscape for the Horiuti-Polanyi dehydrogenation mechanism over Pt and PtSn alloys. In it, we see clearly that initial C-H bond activation following adsorption is the highest energy transition state and rate-limiting step (17).

Given the long history of industrial dehydrogenation reactions, there is a wealth of empirical data available in the literature that describes the reaction kinetics. This reaction is generally carried out at high temperatures and low pressures, leading to low site coverage and allows the use of power law expressions for the reaction rate. (18) (19). The following is one empirical rate law that has been developed for catalysis over supported Pt.

$$-r_A' = k_1 a(t)\left(C_{Propane} - \frac{C_{Propene} C_{H_2}}{K_{eq}}\right)$$

Equation 1 - General rate law for alkane dehydrogenation over platinum catalysts

Where $-r_A'$ is the reaction rate per unit mass of catalyst, k_1 is the rate constant, K_{eq} is the equilibrium constant, and a(t) is the catalyst activity. The catalyst activity, a(t), varies between 1 and 0, and is a

function of time that can be different between different catalyst systems. Empirically, it has been shown that dehydrogenation over metal catalysts typically shows first-order deactivation kinetics (19). Integration of this first order deactivation rate leads to Equation 2

$$\frac{da}{dt} = -k_d a, \qquad a(t) = e^{-k_d t}$$

Equation 2 - First order deactivation equation

Analytical solutions for reactor performance (conversion) as a function of time are only possible for a few simple cases. For example, combining first-order deactivation kinetics and first-order reaction kinetics, the following can be derived describing the impact of deactivation on the conversion in packed bed reactors (19) (20).

$$\ln\left[\frac{1 - X_A}{X_A}\right] = k_d t + \ln\left[\frac{1 - X_{A0}}{X_{A0}}\right]$$

Equation 3 - PDH reaction model including first order deactivation kinetics

Equation 3 allows us to calculate a deactivation parameter, k_d, by plotting the left-hand side vs time for each catalyst system.

Origins of deactivation and selectivity

Deep dehydrogenation and alkane cracking

Until now, we have only considered the reaction pathway of interest in the generation of light olefins. One of the biggest practical concerns for catalyst selection is general stability and resistance to deactivation. Figure 10 below shows propane conversion over commercial Pt-Sn/Al_2O_3 catalysts. Note the rapid deactivation of catalyst leading to falling conversion over time. This behavior is typical of PDH catalysts and presents challenges for their incorporation in industrial processes where catalyst life is often a key factor in the profitability of processes.

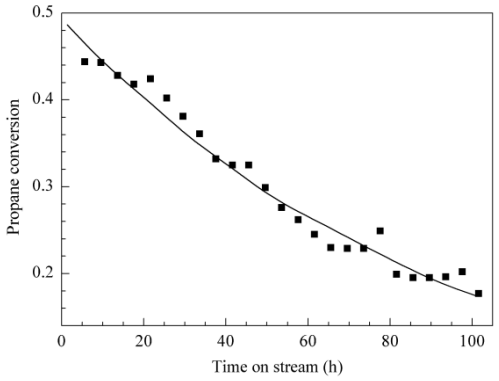

Figure 10 – Deactivation in commercial PDH catalysts. Reaction conditions: T=620°C, H_2/Propane ratio = 0.6, WHSV = $2h^{-1}$. Reprinted with permission from (21).

After adsorption of reactants on to the catalyst surface, there are several pathways that can result in undesired reactions. For example, sequential dehydrogenation steps of the substrate molecule can lead to carbon deposition on the catalyst surface obstructing active sites and lead to loss of activity over time. Swaan et al. found that deactivation of supported nickel catalysts for high temperature methane reforming reactions was driven primarily by carbon deposition, though some nickel sintering does occur (22). Deactivation by coking is also the primary deactivation pathway for supported platinum catalysts and there is much active research is focused on rational catalyst design to reduce coking.

One of the major challenges in reducing coke formation due to deep dehydrogenation is that the olefin target molecules are more reactive toward dehydrogenation than the starting alkanes (6) (23). This implies that an ideal catalyst for propane dehydrogenation would be one that weakly adsorbed the target propylene so that the barrier to desorption is small compared to the thermal energy of the system.

Additionally, support effects play a large role in coke formation. For example, catalysts on acidic supports such as silica show more coke formation due to cracking and deep dehydrogenation than those on similar, but less acidic supports such as alumina. Doping of acidic metal oxide supports with alkali metals has also been demonstrated to reduce coking (22). By complexing metals using surface

hydroxyls, the overall acidity of the metal oxide surface is reduced and the catalysts show lower coke formation rates as compared to the un-doped materials.

Another problematic reaction in dehydrogenation processes is C-C bond scission. This reaction leads to adsorbed alkane fragments on the surface of the catalyst, which can undergo recombination or further dehydrogenation. This mechanism can lead to the production of undesirable side products during propane dehydrogenation. For example, C-C bond scission in propane can lead to methyl groups on the surface that can combine to form ethane or ethene, resulting in reduced overall yield and selectivity. Resulting ethyl groups can also dimerize to form butane, or continued C-C scission and recombination can lead to progressively larger and larger hydrocarbons. If these large alkanes are unable to desorb from the catalyst surface they will eventually lead to surface fouling and coke formation. Some metals like copper are known to be coke resistant because of facile desorption of resulting hydrocarbons, but are generally not useful for dehydrogenation due to high C-H bond activation barriers on copper.

Particle sintering

In addition to coke formation, another commonly observed catalyst deactivation mechanism is particle sintering. In this case, sintering of small, high specific surface area catalyst particles to form larger domains has the effect of lowering the overall surface area of the catalytically active material. While this is typically considered to be negligible below ~40% of the solid metals melting point, due to the low melting point of copper and high temperatures required for propane dehydrogenation this is a concern for our systems. The most common form of decay law from sintering is second order.

$$r_d = k_d a^2 = -\frac{da}{dt}, \qquad a(t) = \frac{1}{1 + k_d t}$$

Equation 4 - Equations describing second order deactivation kinetics, typical of particle sintering

For second order deactivation kinetics, it can be shown, that (20)

$$(k_d t + 1)\left[\frac{1 - X_{A,0}}{X_{A,0}}\right] = \frac{1 - X_A}{X_A}$$

Equation 5 – Performance expression for a mixed flow reactor with second order deactivation kinetics

This again allows us to calculate a deactivation parameter, k_d, for a given reaction system. Long time-on-stream experiments should allow for the discrimination of first and second order deactivation indicating deactivation by coking or sintering.

Bimetallics

One of the commonly used methods for controlling coking and improving catalyst selectivity is the alloying of additional modifiers with the active metals in the catalyst. These modifiers improve activity and selectivity by impacting many characteristics of the materials, which can be grouped in to three major effects. These include geometric, electronic, and co-catalytic effects.

Geometric

To facilitate coke-free propane dehydrogenation, carbon forming reactions must be controlled. Traditionally, bulk metal catalysts are modified with secondary metals to improve deactivation by coking. To understand the impact of these modifiers, it is illustrative to examine a model system such as Sn- modified platinum catalysts like those used in the Oleflex process. Tin atoms are used to interrupt the platinum crystal surfaces and decrease domain size on the surface of the catalysts. As a result, fewer platinum atoms are available in close proximity to adsorbed propane species. These adjacent platinum atoms are responsible for reactions such as γ-H elimination which lead to unwanted side products and strongly adsorbed species which lead to coke formation (24). Additionally, disrupting large platinum domains which shield internal atoms in bulk crystals has the effect of creating more active sites for these reactions and can increase specific activity.

Electronic

While the catalyst characteristics can be influenced by geometric effects one of the defining characteristics of metals is their ability to interact with surrounding atoms in the support lattice. Addition of electron rich or deficient adatoms to form bimetallics can change the electronic structure of adjacent catalytically active metals. Since adsorption, reaction, and desorption are all strongly influenced by the local electronic structure, this redistribution of electron density can increase or decrease reaction rates considerably. This behavior is well described by the d-band theory, which was discussed previously. As an example, Liao et al. showed that interstitial doping of Pd with boron atoms could greatly improve the selectivity for partial hydrogenations. They attributed this improvement to a downshift in the d-band position of B doped Pd without impacting the geometric configuration of the Pd surface.

Cocatalysts

Introduction of additional metals to the catalyst can also provide the opportunity to add new functionality to the system. Deposition or alloying of a second metal can provide new sites with different adsorption properties, or active sites that can change the reaction pathways and accessible transition states. In some cases, catalytically active species can be made from two metals that are not catalytically active alone. Batista et al. demonstrated activity for nitrate reduction over Pd-Cu bimetallics despite finding no activity for either monometallic analog (25).

Single atom alloys

By taking the bimetallic advantages discussed above to their highly-dispersed limit, our research group has made a number of single atom alloys that show interesting catalytic properties. These catalysts exploit the advantages of bimetallics discussed above and have been demonstrated for highly selective partial hydrogenations and dehydrogenations (26) (27). By introducing catalytically active metal atoms

in inert and inexpensive support metals, such as copper, we hope to develop new coke resistant catalysts for general C-H bond activation and propane dehydrogenation (PDH).

There are several synthetic routes to single atom alloys described in the literature, but we have chosen to focus on galvanic replacement methods. These reactions take advantage of the favorable redox chemistry between salts of many transition metals and Cu^0.

$$Pt^{+2}_{(aq)} + 2e^- \rightarrow Pt_{(s)}, \quad E^0 = +1.2V \quad \text{REACTION 1}$$

$$Pd^{+2}_{(aq)} + 2e^- \rightarrow Pd_{(s)}, \quad E^0 = +0.987V \quad \text{REACTION 2}$$

$$Ni^{+2}_{(aq)} + 2e^- \rightarrow Ni_{(s)}, \quad E^0 = -0.25V \quad \text{REACTION 3}$$

$$Cu(s) \rightarrow Cu^{+2}_{aq} + 2e^-, \quad E^0 = -0.34V \quad \text{REACTION 4}$$

Here, we see that Pt^{+2} and Pd^{+2} are strong enough oxidizers to deposit on the surface of Cu^0 NPs. Combinations of Reaction 1 or 2 with Reaction 4 give the following spontaneous redox couples.

$$Pt^{+2}_{(aq)} + Cu(s) \rightarrow Pt_{(s)} + Cu^{+2}_{aq}, \quad E^0 = +0.86V \quad \text{REACTION 5}$$

$$Pd^{+2}_{(aq)} + Cu(s) \rightarrow Pd_{(s)} + Cu^{+2}_{aq}, \quad E^0 = +0.647V \quad \text{REACTION 6}$$

Thus, by adding aqueous solutions of Pt and Pd ions to dispersions of Cu-NPs, we expect to distribute Pt^0 or Pd^0 on the NP surface. However, $Ni^{+2}_{(aq)} + Cu(s) \rightarrow Ni_{(s)} + Cu^{+2}_{aq}, \quad E^0 = -0.59V$ shows that aqueous nickel ions are incapable of spontaneous deposition on the Cu^0 surface.

$$Ni^{+2}_{(aq)} + Cu(s) \rightarrow Ni_{(s)} + Cu^{+2}_{aq}, \quad E^0 = -0.59V \quad \text{REACTION 7}$$

To achieve NiCu SAAs by galvanic replacement, we must operate under basic conditions.

$$Cu_2O + H_2O + 2e^- \rightarrow 2Cu + 2OH^-, \quad E^0 = -0.36V \quad \text{REACTION 8}$$

Combination of Reaction 7 and Reaction 8 give a spontaneous reaction which can be used for CuNi synthesis as reported by Shan et al. (27).

$$2Cu + 2OH^{-} + Ni^{+2} \rightarrow Cu_2O + Ni + H_2O, \quad E^0 = +0.103V \text{ REACTION 9}$$

The resulting catalysts consist of isolated metal atoms dispersed on a copper surface. Atomic-resolution STEM images and CO-FTIR show that these atoms remain atomically dispersed even after heating to 400°C.

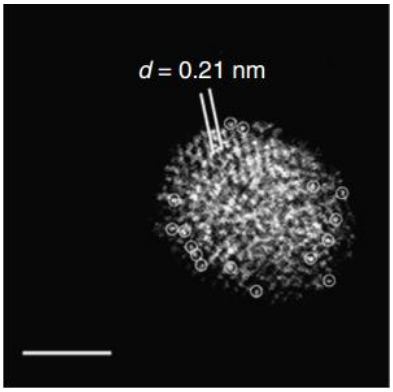

Figure 11 – Aberration corrected HAADF-STEM image of PtCu-SAAs showing isolated Pt atoms on Cu-NPs. Isolated Pt atoms are highlighted with circles. Reprinted with permission from (26).

Thesis objectives

Overall, the largest problem facing existing catalyst systems is their rapid deactivation due to coking. In the case of UOP's Oleflex process, additional cost and risk are associated with their CCR process where deposited coke is burnt off and Pt is redistributed using chlorine at elevated temperatures (28). Additionally, catalyst inventories are kept artificially high by a need to regenerate spent catalyst in real time during the process. For the Catofin process, entire reactor trains are brought in and out of service to regenerate catalyst whose deactivation is primarily driven by coking. In a typical configuration 5 reactor configuration, at any time, one reactor is undergoing regeneration requiring significant excess capital expenditure to meet a target production rates (6).

The work presented in this thesis is primarily concerned with the rational design of single atom alloy catalysts for potentially coke resistant C-H bond activation catalysts in butane and in propane dehydrogenation reactions as there is significant economic upside in reducing the regeneration frequency of industrial catalysts. By extending previously described catalytic trends to the single atom limit, we hope to make improvements over existing systems. Additionally, more fundamental studies are required to demonstrate the applicability of SAA catalysts for alkane dehydrogenation. To the best of the author's knowledge, no studies have yet demonstrated that these reactions can take place over single isolated metal atoms on inert supports. Similarly, there are no literature results available for comparison of apparent activation energies for alkane dehydrogenation over SAAs as compared to their monometallic nanoparticle analogs.

To this end, the following objectives were identified for this thesis work.

1. Demonstrate activity for C-H bond activation and PDH reactions over SAA catalysts.
2. Confirm that copper supports with low product desorption barriers limit coke deposition and deactivation.
3. Measure deactivation kinetics to discriminate between particle sintering and deactivation by coking.
4. Measure apparent activation energies over each catalyst to compare reaction pathways for SAA catalysts with their monometallic nanoparticle analogs.

To address these objectives single atom Pt, Pd, and Ni on silica supported Cu and their monometallic nanoparticle analogs were prepared for catalytic studies. Following particle characterization, C-H bond activation experiments were carried out using H-D bond scrambling between butane and deuterium gas, and PDH reactions were carried out under representative conditions. Reaction rates were calculated and Arrhenius plots were used to calculate apparent activation energy for each catalyst system. Deactivation kinetics were studied using two models – one typical of deactivation by sintering, and another typical of coking and primary deactivation routes are proposed for each system. Using these samples, coke analysis was carried out using temperature programmed oxidation and the coke

composition and total deposition was compared for each catalyst system. Finally, spent catalysts were analyzed using carbon monoxide diffuse reflectance infrared Fourier transform spectroscopy (CO-DRIFTS) to determine the impact of the applied reaction conditions on the SAA catalysts.

Chapter 2 - Experimental Methods and Procedures

Catalyst preparation

Supported copper nanoparticle preparation

Supported copper nanoparticles were synthesized following the procedure previously described by Boucher et al (29). In this synthesis, copper nanoparticles (Cu-NPs) were prepared as colloids by reducing a copper precursor in solution using sodium borohydride ($NaBH_4$) as the reducing agent, and polyvinylpyrrolidone (PVP, MW 40,000) as a capping agent to prevent particle agglomeration during synthesis. In a typical preparation, an aqueous solution of 0.01M $Cu(NO_3)_2$ was added to a flask containing PVP, and citric acid was added giving a 200:1 Cu:PVP molar ratio. The solution was sparged with N_2 for 60 minutes followed by constant N_2 purge for the remainder of the reaction. After mixing, the light blue solution turns light red. An aqueous solution of $NaBH_4$ was added to reduce the nanoparticles giving a 2:1 molar ratio of Na:Cu, which produced an opaque brown suspension. The resulting nanoparticles were deposited onto a silica support (fumed silica, 0.2-0.3 µm average aggregate particle size, surface area 200 m^2/g) by adding an aqueous silica dispersion dropwise to the Cu-NP suspension. The sample was vacuum filtered, washed with water, and dried under vacuum. The supported Cu-NPs were then calcined at 300^oC by heating at 5^oC/min, holding for 4 hours, and cooling to room temperature to remove the PVP capping agent, yielding oxidized Cu-NPs supported on fumed silica (29).

PtCu and PdCu SAA preparation

Starting from the supported Cu-NPs described above, platinum and palladium single atom alloys were prepared by galvanic replacement. In a typical synthesis 2g calcined silica supported Cu-NP (3.6 wt% Cu by ICP) was loaded in to a quartz tube. The copper nanoparticles were reduced in 5% H_2/N_2 by heating

to 300°C at 2°C/min. They were maintained at 300°C for 3 hours, then cooled to room temperature at 2°C/min.

A round bottom flask containing 150mL deionized water was sparged with N_2 at 90°C and was kept under N_2 flow for the remainder of the reaction. The pre-reduced Cu-NPs were added to the flask, followed by 2-3 drops 10% HCl. 5mg $Pd(NO_3)_2*xH_2O$ was dissolved in a minimum amount of water, and the solution was added dropwise to the stirring Cu-NP dispersion. After stirring at 90°C for 1 hour, the solution was cooled, vacuum filtered, and washed with ~5L of water. Collected samples were dried under vacuum for several days.

NiCu SAA preparation

Starting from the supported Cu-NPs described above, nickel-copper single atom alloys were prepared using the modified galvanic replacement method described by Shan et al (27). In a typical synthesis, 2g Cu/SiO_2 was reduced as in the PtCu and PdCu case. 6mg $Ni(NO_3)*6H_2O$ was added to the flask. The reaction was sparged with N_2 and was kept under N_2 flow for the rest of the reaction. The pH was adjusted to 10.85 using 0.1M NaOH. The pre-reduced Cu-NPs were then added to the solution. After stirring for 1 hour, the sample was vacuum filtered and washed with ~5L of water. Collected samples were dried under vacuum for several days.

Preparation of monometallic catalyst by incipient wetness impregnation

Monometallic Pt, Pd, and Ni catalysts were prepared using an incipient wetness impregnation method. In a typical synthesis, 0.2-0.3µm fumed silica was calcined at 650°C for 4 hours. 1.2g calcined silica was loaded into a 50mL conical tube. 0.15g $Pd(NO_3)_2$ was dissolved in 0.66mL water and this solution was added dropwise to the conical tube with vigorous mixing. The sample becomes notably denser during water addition, reducing to approximately half of its original volume. After the aqueous solution was

added, the sample was dried under vacuum for several days. The samples were calcined by heating at 2°C/min to 300°C, held for 4 hours, then cooled to room temperature at 2°C/min.

Catalytic testing

Temperature programmed reduction (TPR), C-H bond activation, and PDH

Prior to use in C-H bond activation and PDH reactions, catalysts were pre-reduced in situ. In a typical preparation, 200mg catalyst was diluted with 1g calcined quartz bead and was loaded into a 1cm diameter cylindrical quartz reactor tube with quartz wool to secure the plug. The reactor tube was loaded into a clam shell furnace equipped with temperature control. The sample was purged for 20 minutes with 50mL/min 20% H_2/He. The sample was reduced using this same flow rate by heating at 5°C/min to 400°C (for C-H bond activation) or 550°C (for PDH). The catalysts were reduced for 2 hours, then they were cooled to room temperature at 5°C/min. Reactor effluent was monitored by mass spec. During TPR, m/z=2,4,18 were monitored to measure H_2 consumption and water production due to metal oxide reduction.

After cooling to room temperature, the desired flows were set using MFCs or metering valves and the flow rates were manually checked using a bubble flow meter. In a typical butane C-H bond activation experiment, the following flow rates were established.

Table 3 - Typical gas flow rates and concentrations for butane C-H bond activation work

Gas	Flow rate (mL/min)	Mol %
Argon	48	92.8
Butane	2.3	4.5
D2	1.4	2.7
Total	51.7	-

For a typical PDH reaction, the following gas flows were used.

Table 4 - Typical gas flow rates and concentrations for PDH reactions

Gas	Flow rate (mL/min)	Mol %
Helium	48	80
Hydrogen	6	10
Propane	6	10
Total	60	-

After establishing the gas flows, the reactor was allowed to equilibrate and purge for 1 hour. Once a stable baseline had been reached, the desired temperature program was set, and the reactor was heated. A typical heating profile for long time-on-stream experiments is presented in Figure 12 below.

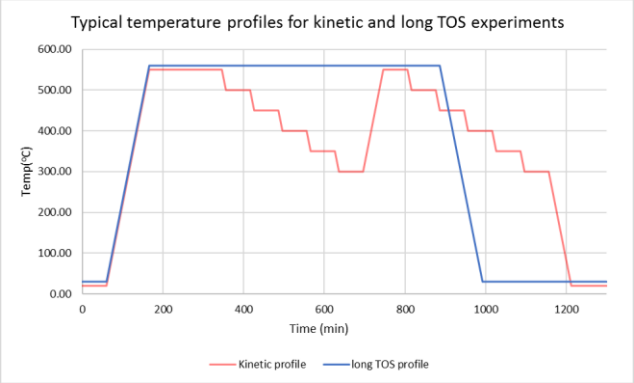

Figure 12 - Typical temperature profile for propane dehydrogenation reactions. Data offset for clarity.

Characterization Methods

Carbon monoxide diffuse reflectance infrared Fourier transform spectroscopy (CO-DRIFTS)

To confirm the formation of nanoparticles with isolated metal atoms, CO chemisorption and FTIR was used to discriminate between CO adsorbed atop a single metal atom and CO occupying a bridged site between two adjacent surface sites. CO chemisorption and FTIR was carried out on a Thermo Nicolet iS50 FT-IR equipped with a Harrick DRIFTS cell. CO-FTIR was performed for fresh and spent catalysts to determine impact of real reaction conditions on catalyst stability with respect to metal aggregation. In a typical preparation, a small flow through FTIR cell was loaded with catalyst and packed firmly to develop a small plug. The FTIR cell was assembled, and the sample was reduced in 20% H_2/He at 400°C. The

sample was returned to room temperature and a background spectrum was collected for the background subtraction. After the background spectrum was collected, the sample was exposed to a 100% CO flow for 10 minutes. After CO exposure, the reactor was purged with 100% He. After 5 minutes of He purging, an IR spectrum was obtained every 3-5 minutes to monitor the desorption of CO from the catalyst surface.

Extended X-Ray absorption fine structure (EXAFS)

EXAFS was used to determine the coordination environment of Pt atoms on PtCu SAAs and a Pt foil reference. The spectra were obtained at beamline 12-BM at Applied Photon Source (Argonne National Laboratory). The samples were pre-reduced in H_2 at 400 °C in situ. Then XAS spectra are collected in helium at ambient temperature. XAS data was processed and analyzed using Athena and Artemis. EXAFS spectra were plotted in k-space and R-space for comparison of SAAs and bulk Pt foil.

Inductively coupled plasma atomic emission spectroscopy (ICP-AES)

Metal content of catalyst samples was measured using ICP-AES. In a typical preparation 50mg catalyst was dissolved in 2mL 37% HCl and 5 drops of 35% H_2O_2. After vigorous stirring for several minutes, the sample was brought to ~20mL with DI water and was left uncovered for 2 days to allow for H_2O_2 decomposition. Finally, the sample was brought to 50mL in a volumetric flask. This solution was used directly for ICP-AES analysis. Cu, Pt, Pd, and Ni metal standards were prepared from 1mg/mL stock solutions available from Sigma-Aldrich.

Temperature programmed oxidation (TPO) of spent catalysts

To characterize and compare the coke deposits on each of the catalysts studied, temperature programmed oxidation was carried out on the spent catalyst that was used in the long time-on-stream experiments. In a typical TPO reaction, catalyst samples were exposed to butane C-H bond activation conditions at 360^{o}C for 12 hours or PDH conditions at 550^{o}C for 12 hours to yield the spent catalyst.

Approximately 100mg spent catalyst was loaded into a 1cm diameter quartz tube. The plug was secured with quartz wool, and the tube was loaded in to the tube furnace. Before oxidation, the samples were pretreated at 300^{o}C for 2 hours with 50mL/min argon flow to desorb any volatile hydrocarbons. After cooling to room temperature, the gas flow was switched to 20mL/min 20% O_2 in He. The samples were heated to 600^{o}C at a ramp rate of 3^{o}C/min. CO_2 evolution was measured by monitoring m/z=44 with mass spec.

Chapter 3 – Activation of C-H bonds

With the shale gas boom in the United States continuing to create low cost light alkanes as starting materials for more complex chemicals much attention is being paid to opportunities to activate these relatively inert compounds for conversion to value added products (30) (31). As the first step toward the production of many fuels and fine chemicals, facile C-H bond activation establishes itself as a critical pathway to improving global production light alkane derivatives. For example, C-H bond activation in alkanes during dehydrogenation reactions produces alkenes. These facts have led to long standing interests in catalytic approaches to C-H bond activation and alkane functionalization. However, C-H σ bond stability, large ionization energy, very small of dipole moment and very high pK_a of alkanes make them very resistant to most chemical functionalization routes (31).

Although researchers have gone to great lengths to improve dispersion and activity of active sites in heterogeneous catalysts only a small portion of the active metal is typically involved in catalysis (32). By taking these efforts to their logical end, single atom metal catalysts have the potential to provide significant benefits over existing commercial catalysts (33) (34) (35). Low coordination number metal centers (36) (37), quantum effects associated with electron confinement (38), metal-support interactions from chemical bonding, and charge transfer between metal species all show exciting impacts on catalyst reactivity (39).

Platinum has long been used as a catalyst for C-H bond activation in alkanes. These materials have found use in dehydrogenation reactions, methane reforming, and coupling reactions to form C-C and C-N bonds (40). One common approach to probing the reaction pathways and kinetics in reactions over heterogenous catalysts is to introduce deuterium as a method to discriminate between H atoms directly involved in reaction pathways, and those that are spectators (41). Under C-H bond activation conditions, recombination of alkyl fragments with surface H or D can lead to incorporation of co-fed D_2

in to the reaction substrate. In the case of reactions with butane and D_2 rapid dehydrogenation/hydrogenation steps will lead to a distribution of isotopologues which reflect the thermodynamic intricacies of many competing reaction mechanisms. Indeed, it has been suggested that while these reactions are dominated by the Horiuti-Polanyi mechanism, careful experimental design has even demonstrated evidence of a "reverse" Eley-Rideal mechanism in which a gas phase alkene reacts directly with two surface adsorbed deuterium atoms (42). Mass spectrometry is typically used to monitor either H-D production from adsorption-scrambling-desorption reactions or the isotopologue distribution of the substrate molecule to gain insight in to the underlying mechanism.

In our experiments, C-H bond reactions were studied over Cu-NPs, Pt-NPs, and PtCu-SAAs. These were used as a model system to verify that C-H bond activation in alkanes over single atom catalysts was possible, and to confirm unpublished surface science results from the Sykes group at Tufts University that the PtCu-SAA system should be coke resistant when compared to their monometallic analogs. Here, we fed D_2 and butane to our reactor and monitored the C-H bond activation reaction by observing the production of butane-d_1 (m/z=59) by mass spectrometry. After confirmation of catalyst activity, we performed TPO experiments to compare coke deposition on each catalyst. Finally, CO-DRIFTS was used to determine the impact of reactor conditions on our SAA catalysts.

A summary of the samples prepared for catalyst studies is presented below in Table 5. The following sections will discuss the individual analytical measurements for all catalysts, including those used only in the PDH work as it makes more sense to consider them together.

Table 5 - Summary table of catalysts used in C-H bond activation and PDH reactions

Sample	Composition	Preparation Method	Metal state
Cu-NP	3.6 wt% Cu on SiO_2	Colloidal	
Pt-NP	0.5 wt% on SiO_2	IWI	Single atom, clusters, and NP's
Pd-NP	0.1 wt% on SiO_2	IWI	Assumed Single atom, clusters, and NP's
Ni-NP	0.1 wt% and 1.8 wt% on SiO_2	IWI	Assumed Single atom, clusters, and NP's
$Pt_{0.03}$Cu-SAA	0.3 wt.% Pt, 3 wt.% Cu on SiO_2	GR	Single atoms on Cu surface by EXAFS
$Pt_{0.01}$Cu-SAA	0.1 wt.% Pt, 3.4 wt.% Cu on SiO_2	GR	Single atoms on Cu surface by EXAFS
$Pd_{0.01}$Cu-SAA	0.2 wt% Pd, 6.5 wt% Cu on SiO_2	GR	Single atoms on Cu surface by CO-DRIFTS
$Ni_{0.005}$Cu-SAA	0.1 wt% Ni, 6.5 wt% Cu on SiO_2	GR	Single atoms on Cu surface by CO-DRIFTS

CO-DRIFTS and EXAFS

PtCu single atom alloys

To determine the dispersion of catalytically active metals on the Cu surface and confirm the formation and stability of SAA catalysts, CO-DRIFTS was used. Figure 13 below shows the CO-DRIFTS spectra taken after reduction of fresh $Pt_{0.01}$Cu-SAA and the same sample after exposure to C-H bond activation conditions for butane (360°C). Figure 14 shows similar spectra for the $Pt_{0.03}$Cu-SAA sample after exposure to C-H bond activation conditions with butane (360°C), and PDH conditions (550°C).

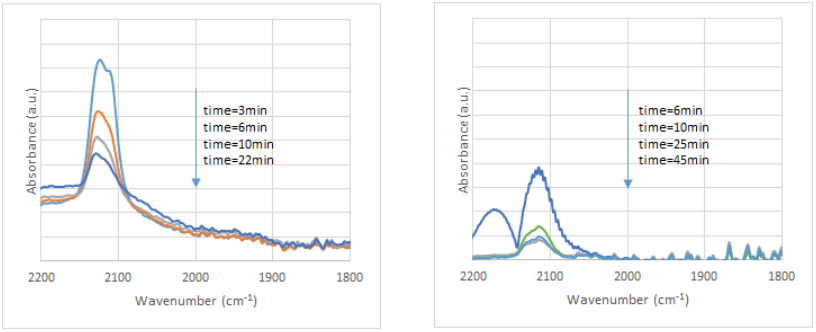

Figure 13 - FTIR spectra of chemisorbed CO on $Pt_{0.01}$Cu-SAA(left) and $Pt_{0.01}$Cu-SAA after 12 hours under Butane-D2 scrambling conditions (right). Time values on the graph indicate the time of helium purge after CO exposure.

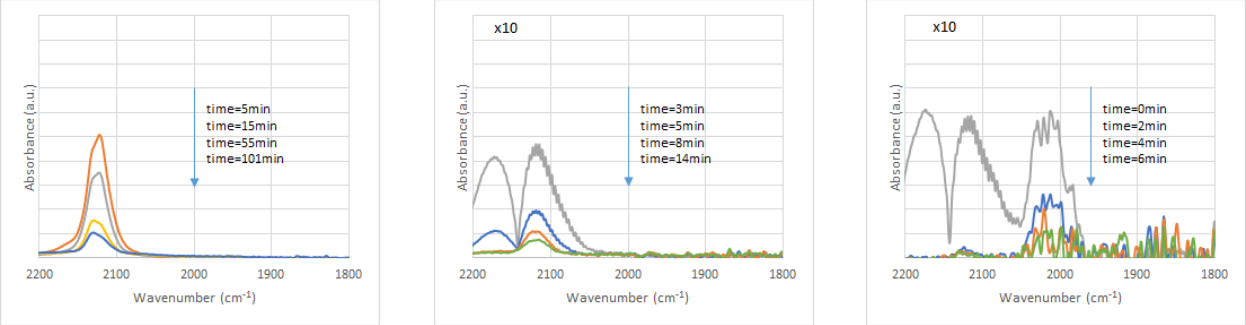

Figure 14 - FTIR spectra of chemisorbed CO on Pt0.03Cu-SAA (left), after 12 hours under Butane-D2 scrambling conditions (Center), and after 12 hours under PDH conditions (right). Time values on the graph indicate the time of helium purge after CO exposure.

Figure 13 and Figure 14 show characteristic peaks at 2130 to 2112 cm^{-1} , which are assigned to adsorbed CO on Cu or Pt sites (43) (44) (45). Typical peaks corresponding to linearly adsorbed CO and bridging CO on extended Pt surfaces, which appear at 2018-2043 cm^{-1} and 1780-1820 cm^{-1} respectively (46) (47), are not observed in fresh samples. This suggests that Pt atoms are fully dispersed and dilute on the copper surface. Additionally, the CO peaks are not shifted as the CO coverage is decreased, which indicates small or no dipole-dipole interactions between nearby adsorbed CO molecules due to high Pt dispersion on the copper surface (48) (43). Spectra collected after Butane-D_2 scrambling reactions show no major changes after 12 hours on stream with either catalyst. This is consistent with highly stable PtCu-SAAs, which show no major aggregation of Pt atoms on the copper surface.

Following exposure to PDH conditions at 550°C, some changes to the catalyst structure were observed. First, total CO adsorption is largely reduced, likely due to coke formation or particle sintering, reducing the number of exposed metal sites. The formation of a peak around 2015cm^{-1} is indicative of linearly adsorbed CO on Pt, with evidence of a small, broad peak centered around 1865cm^{-1} which is assigned to bridging CO on Pt (47). Difficulty in obtaining good spectra for spent catalyst sample makes the analysis

challenging, and EXAFS analysis is needed to develop a good picture of the high temperature stability of these spent catalysts to dehydrogenation conditions.

Figure 15 below shows the EXAFS of $Pt_{0.01}$Cu-SAA, $Pt_{0.03}$Cu-SAA and Pt foil plotted in k-space and Fourier transform space (R-space). $Pt_{0.01}$Cu-SAA and $Pt_{0.03}$Cu-SAA show Pt/Cu interaction peak at lower R value in comparison to that of Pt-Pt interaction peak of Pt foil. EXAFS model fitting suggests there is no Pt-Pt interaction in $Pt_{0.01}$Cu-SAA or $Pt_{0.03}$Cu-SAA in the first coordination shell but only in Pt/Cu interactions (Table 6). This further confirms that Pt atoms are fully isolated in the Cu nanoparticles. The Pt-Cu interaction distance in the first coordination shell (2.59 and 2.61 Å) is greater than that of Cu-Cu (2.56 Å) and lower than that of Pt-Pt (2.76 Å). This is consistent with the formation of SAAs (26).

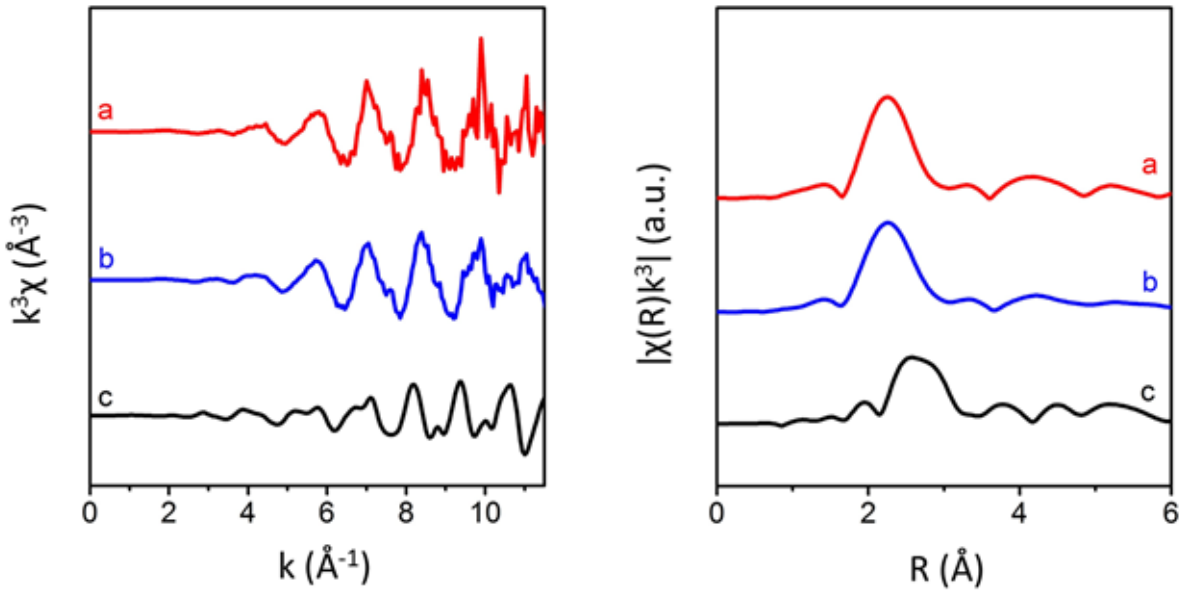

Figure 15 - In situ Pt L_{III} EXAFS of (a) $Pt_{0.01}$Cu-SAA, (b) $Pt_{0.03}$Cu-SAA and (c) Pt foil plotted in k space (Left). Fourier transforms of k^3-weighted Pt L_{III} EXAFS of (a) $Pt_{0.01}$Cu-SAA, (b) $Pt_{0.03}$Cu-SAA and (c) Pt foil plotted in R space.

Table 6 - [a] CN, coordination number. [b] R, distance between absorber and backscattered atoms. R-factor, closeness of the fit, if < 0.05, consistent with broadly correct models.

Sample	Shell	CN[a]	R[b] (Å)	σ^2 (Å^2)	R-factor
Pt foil	Pt-Pt	12	2.764±0.002	0.004	0.001

Pt0.012Cu-SAA	Pt-Pt	0			0.013
	Pt/Cu	10.51±1.62	2.591±0.004	0.005	
Pt/Cu	Pt-Pt	0			0.016
	Pt/Cu	10.80±1.75	2.609±0.004	0.006	

Due to infrequent access to the beam line for XAFS measurements, we were unable to analyze the PdCu-SAA and NiCu-SAA samples prior to the writing of this report.

PdCu single atom alloys

Pd was examined as an alternative minority species to Pt. Similar CO-DRIFTS experiments were carried out for $Pd_{0.01}Cu$-SAAs. Figure 16 below shows the resulting CO-DRIFTS spectra for the samples before and after 12 hours at PDH conditions (550^{o}C). The fresh catalyst shows a single apparent peak at 2120 cm^{-1} with some asymmetry, consistent with CO adsorption on Cu and atomically dispersed Pd atoms showing CO adsorption at 2088 cm^{-1} (49) (50). No significant peaks are noted corresponding to linear or bridging CO adsorption on extended Pd surfaces, although Sitthisa et al have demonstrated that even at relatively high loadings in a $Pd_{0.5}Cu_2/SiO_2$ alloy, linear and bridging CO peaks attributed to Pd are low intensity (49). As is the case with PtCu SAAs, EXAFS spectra are needed to confirm the final state of Pd dispersion on these catalysts as weak signal and difficulty in discriminating Cu and dispersed Pd on the samples makes definitive identification difficult. The peak which develops at 2020cm^{-1} is not consistent with extended Pd surfaces on copper (49), silica (51), or our own Pd-NPs, and currently remains unassigned

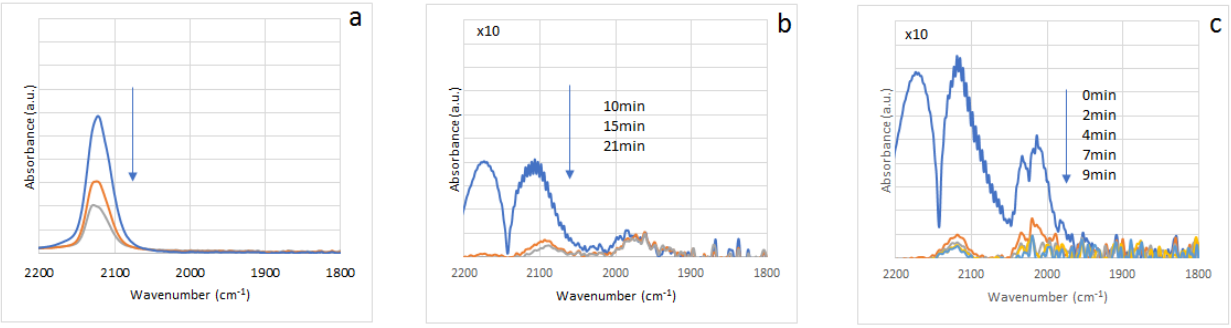

Figure 16 - CO-DRIFTS spectra for fresh PdCu-SAAs (a) fresh Pd-NPs (b) and PdCu-SAAs after exposure to PDH conditions (c). Time values on the graph indicate the time of helium purge after CO exposure.

NiCu single atom alloys

CO-DRIFTS spectra for $Ni_{0.01}Cu$-SAAs are presented below in Figure 17. The freshly reduced catalyst shows some evidence of peak asymmetry on the low wave number side which is assigned to low levels of Ni doped in the Cu surface. The asymmetry is likely due to a small band at 2110cm^{-1} which is obscured by the CO stretch on Cu^0 and Cu^+ (27). The spent samples show the development of a broad peak at 2005 cm^{-1}, which is assigned to linearly adsorbed CO on Ni sites (52). Again, EXAFS analysis is needed to complement the CO-DRIFTS work and determine the structural effects and catalysts stability after operation at high temperature in reducing atmospheres.

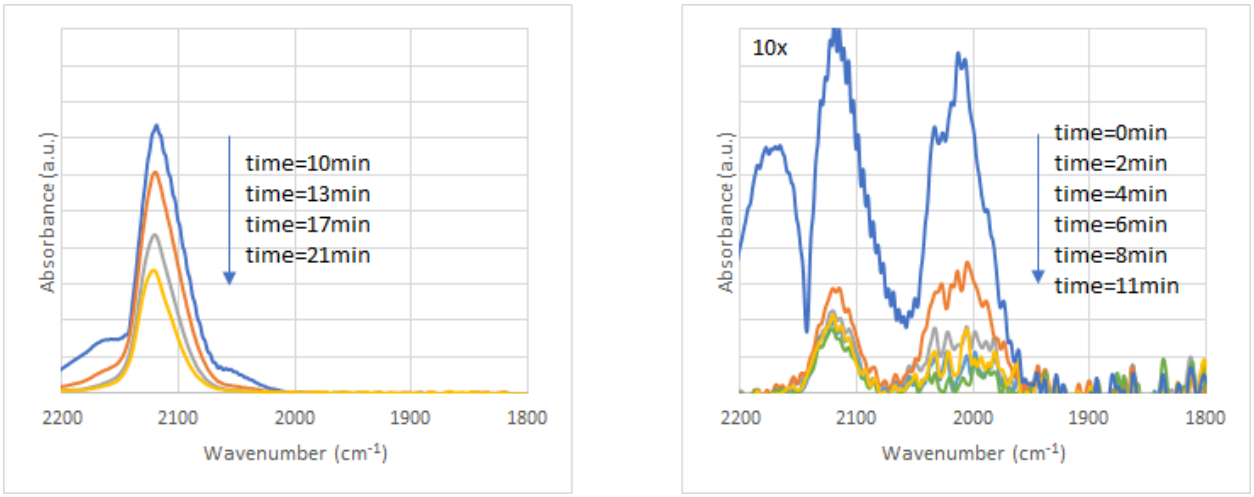

Figure 17 - CO-drifts spectra for fresh NiCu-SAAs (left) and NiCu-SAAs after exposure to PDH conditions (right). Time values on the graph indicate the time of helium purge after CO exposure.

Temperature programmed reduction (TPR)

Temperature programmed reduction of each sample was carried out prior to PDH reactions. Using H_2 as the reducing agent, samples were heated to 550°C and the reduction reaction was followed by mass spectrometry monitoring water production.

$$CuO + H_2 \rightarrow Cu + H_2O \quad (6)$$

The reduction of copper proceeds at a characteristic temperature by surface H atoms. This reaction temperature can be influenced by the addition of adatoms capable of H_2 adsorption and dissociation, which is well demonstrated in the literature. This allows for the identification of copper oxide reduction peaks and for the comparison of the H_2 adsorption and activation by observing the shift in temperature. Metals exhibiting facile H_2 activation are expected to promote the reduction of copper oxides at lower temperatures (53) (15) (19) (25). Figure 18 below shows the TPR profile for the Cu-NPs on which all of the SAAs in this study were made.

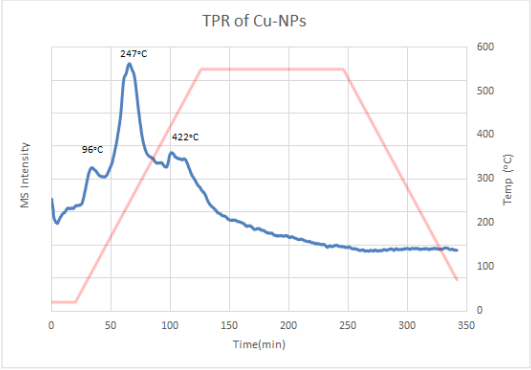

Figure 18 - TPR profile for supported Cu-NPs. 20% H_2/bal He. 50mL/min total flow. Temperature ramp = 5°C/min.

Three major peaks are observed in Figure 18. The low temperature peak at 96°C is due to surface adsorbed water, while the high temperature region starting around 422°C is attributed to the thermal dehydroxylation of silica. Although the silica support was calcined before use in NP synthesis, complete removal of surface silanols is difficult without rigorous drying, and formation of new silanols from

strained siloxanes is possible even at the room temperature (54). These two peaks are present in all of the prepared samples.

The final peak present in Figure 18 at 247°C is attributed to copper oxide reduction to Cu^0. This temperature is consistent with the literature (55) and provides a convenient reference peak for catalyst samples.

Pt and PtCu reduction

For TPR of supported Pt catalysts, the literature suggests we should expect reduction of bulk Pt at low temperatures. Figure 19 below shows a small reduction peak at 60°C, which is attributed to the reduction of Pt on the SiO_2 surface, and this generally agrees with values reported in the literature (56). We also see a shift of the major CuOx reduction peak from 247°C to 211°C.

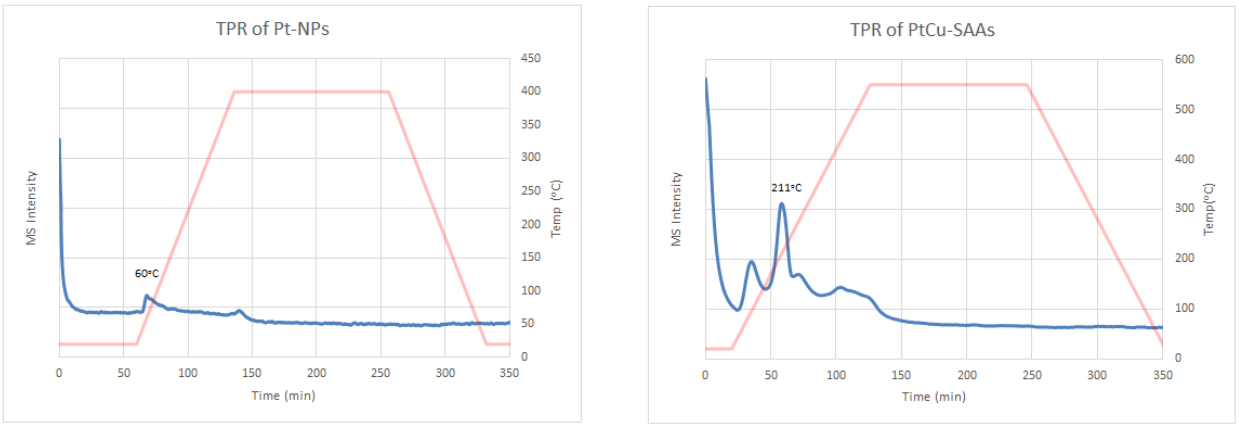

Figure 19 - TPR profile for supported Pt-NPs and PtCu-SAAs. The major peak at 211°C is attributed to CuO reduction to Cu^0. 20% H_2/bal He. 50mL/min total flow. Temperature ramp = 5°C/min.

Pd and PdCu reduction

For TPR of supported Pd catalysts, facile reduction of Pd is expected even at room temperature. Negative H_2 consumption due to Pd-H destruction and H_2 desorption around 0°C is well documented (25). Given that we are limited to room temperature using our setup, no reduction peak for Pd is observed for our Pd catalysts. This reduction peak should be observable using a cooled TPR apparatus. Batista et al demonstrated the reduction of PdCu alloys over Al_2O_3 and measured a drop in the CuOx

reduction temperatures after Pd introduction for the pathway to Cu^0. Figure 20 below shows the shift of the major CuOx reduction peak in our PdCu-SAAs from 247°C in Cu-NPs to 196°C.

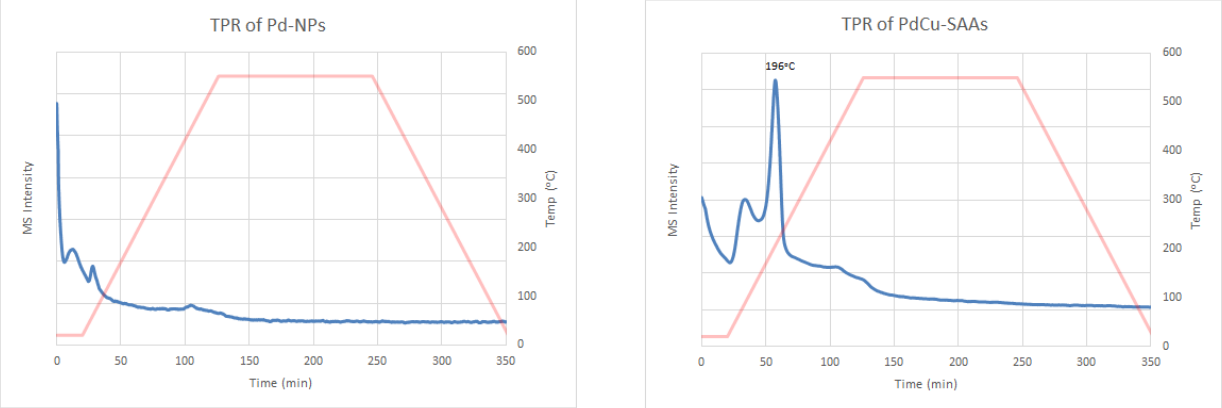

Figure 20 - TPR profile for supported Pd-NPs and PdCu-SAAs. The major peak at 196°C is attributed to CuO reduction to Cu^0. 20% H_2/bal He. 50mL/min total flow. Temperature ramp = 5°C/min.

Ni and NiCu reduction

For TPR of supported Ni and NiCu samples, we see similar trends for shifts in reduction temperatures. Literature values for reduction temperatures for supported Ni-Cu alloys show a range of values associated with each metal with catalyst support playing an important role. Khromova et al reported that reduction of Ni/SiO_2 occurs primarily from 400-450°C with onset as low as 200°C (57). Kang et al. reported reduction onset of Ni/Al_2O_3 at similar temperatures, though with a much lower peak (53). By varying the composition of $Cu\text{-}Ni/SiO_2$ alloys, they were able to show that the addition of copper shifts the reduction of nickel oxides to a lower temperature (57). In Figure 21 below, our Ni-NP catalyst shows the onset of Ni reduction at similar temperatures with a very broad peak attributed to widely dispersed Ni atoms on the SiO_2 surface exposed to a range of chemical environments. This behavior is seen in the NiCu-SAA sample as well with long reduction times and temperatures up to 550°C needed to complete reduction. Cu reduction is found to occur at lower temperatures than bulk Cu-NPs, with the effect of Ni atoms notably less than Pt or Pd.

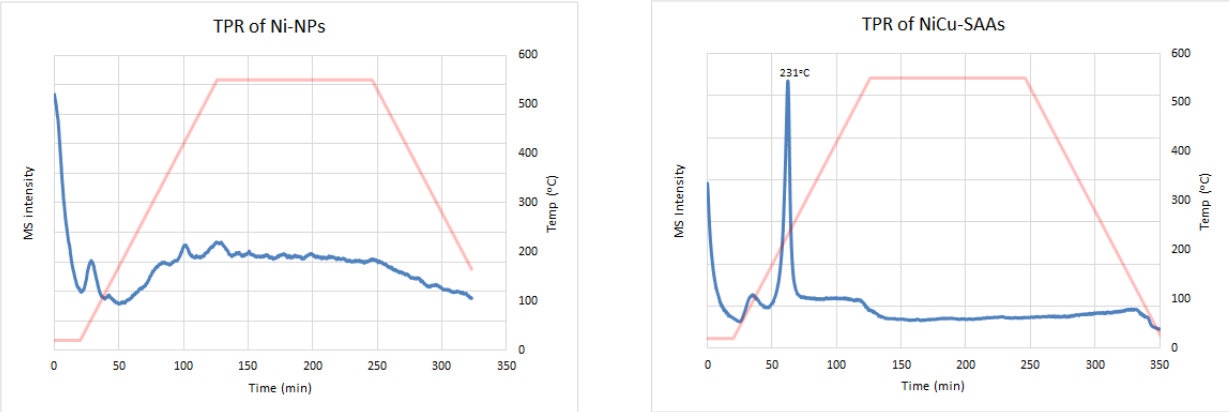

Figure 21 - TPR profile for supported Ni-NPs and NiCu-SAAs. The wide reduction peak is attributed to dispersed Ni atoms on the bulk Cu-NPs. 20% H_2/bal He. 50mL/min total flow. Temperature ramp = 5°C/min.

C-H bond activation in butane

In collaboration with the Sykes group at Tufts University, a series of ambient pressure catalytic C-H bond activation experiments were carried out using the $Pt_{0.01}Cu$ and $Pt_{0.03}Cu$ SAAs previously described. To demonstrate the expected coke resistance of these catalysts, we carried out B-D scrambling experiments at temperatures up to 400^{o}C. After single crystal experiments conducted under ultra-high vacuum (UHV) demonstrated methane and ethane desorption from PtCu SAAs following CH_3I exposure, these reactions were carried out to verify the hypothesis that C-H bond activation could reduce coke formation rates by providing surface H atoms to produce volatile lower alkanes on the catalyst surface from coke precursors (58).

For these tests, we followed the C-H bond activation reaction using mass spectrometry. Dilute butane and deuterium in argon were fed in to the reactor as the temperature was varied and the gas stream was sampled at the outlet for analysis. As butane is adsorbed on to the catalyst surface, C-H bond activation allows for recombination of alkenyl fragments with surface deuterium atoms to produce Butane-D_1. Higher levels of substitution are possible as multiple dehydrogenation/hydrogenation steps are possible with the same butane molecule. In the absence of catalytic activity and H-D exchange, the 59 signal should be a fixed value based on the natural isotopic distribution in butane. This makes the 59/58 ratio a convenient metric for measuring C-H bond activation activity. As the C-H bond activation activity increases, so should the 59/58 ratio.

After reduction in 5% H_2/He, temperature programmed surface reactions (TPSR) were carried out. Figure 22 below shows some of the TPSR data collected for Cu-NPs, $Pt_{0.01}Cu$-SAAs, and $Pt_{0.03}Cu$-SAAs.

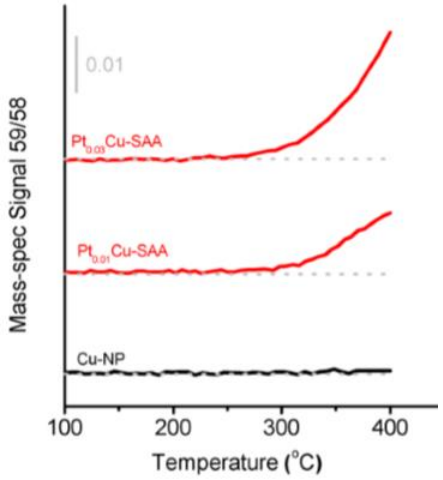

Figure 22 - Second cycle TPSR data for PtCu-SAAs and Cu-NPs. 100mg catalyst. 5% butane/2% deuterium/bal. argon. Total flow rate = 50mL/min. Temperature ramp = 5°C/min.

Figure 22 shows the onset of C-H bond activation activity is shifted to much lower temperatures by the addition of atomically dispersed Pt atoms on the copper support. Indeed, up to 400°C, Cu-NPs show no obvious activity. By further increasing the temperature, we find activity only above 550°C.

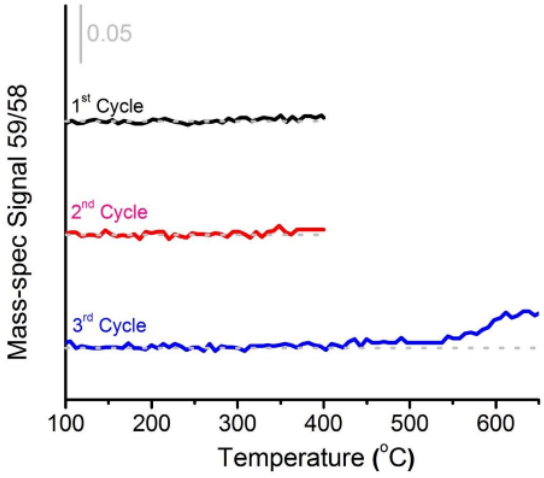

Figure 23 - TPSR data for C-H bond activation in butane over Cu-NPs. 100mg catalyst. 5% butane/2% deuterium/bal. argon. Total flow rate = 50mL/min. Temperature ramp = 5°C/min.

Examination of Pt-NPs shows lower temperature onset of C-H bond activation as expected. However, rapid deactivation during the first cycle for this system is observed, and subsequent TPSR cycles show relatively low activity.

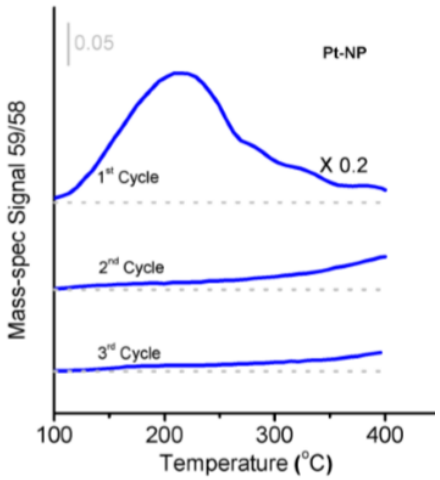

Figure 24 – TPSR data for C-H bond activation in butane over Pt-NPs. 100mg catalyst. 5% butane/2% deuterium/bal. argon. Total flow rate = 50mL/min. Temperature ramp = 5°C/min.

Following TPSR experiments, conditions were chosen for long time-on-stream experiments to evaluate the long-term stability of PtCu SAAs vs Pt-NPs. Samples were reduced as before and the samples were heated to 360°C in the butane/deuterium/argon stream detailed in Table 3.

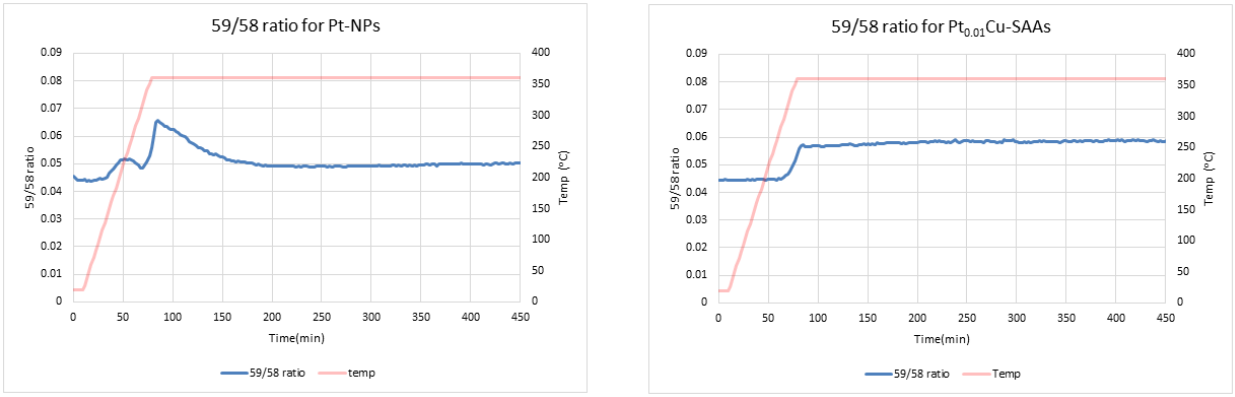

Figure 25 - Long TOS experiments for Pt-NPs (left) and PtCu SAAs (right). 100mg catalyst. 5% butane/2% deuterium/bal. argon. Total flow rate = 50mL/min. Temperature ramp = 5°C/min.

Figure 25 clearly shows the improved stability of the PtCu-SAA as compared to Pt-NPs. In addition to the stability improvements, we see that the long-term conversion is higher for the single atom alloy even with much higher Pt loading by weight in the Pt-NPs. Another interesting feature of the Pt-NPs is the

initial onset of activity at low temperatures, followed by deactivation. This is also observed in the Ni-NP and Pd-NP samples used in propane dehydrogenation (see Figure 29) and is assumed to be activity from specific highly active sites in the particle surface.

Following long time-on-stream experiments, coke analysis was carried out by temperature programmed oxidation. Figure 26 below shows much reduced CO_2 evolution on $Pt_{0.01}Cu$-SAAs (b) as compared to our Pt-NPs catalyst (a). The total coke formation on our Pt-SAAs is similar to that of the silica support (c). Thus we conclude that no carbon deposition took place on the SAAs.

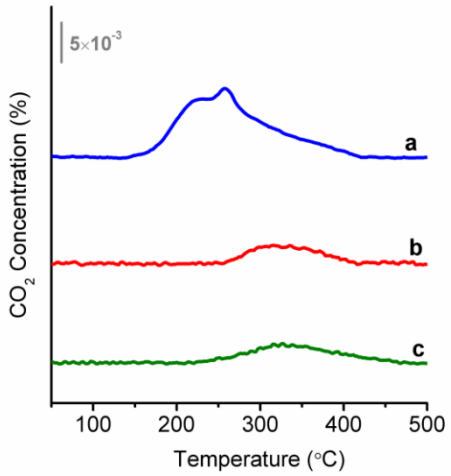

Figure 26 - Comparison of coke deposition by TPO on Pt-NPs (a), PtCu-SAAs (b), and silica support (c). 100mg spent catalyst. Samples purged in Argon at 300°C followed by heating from room temperature to 600°C at 3°C/min using 20% O_2 in Ar, total flow = 50mL/min.

This figure also shows a broad CO_2 evolution peak from Pt-NPs, which is absent from our PtCu-SAAs and support material. Two peaks are discernable, with the second corresponding to graphitic carbon oxidation (59). These results demonstrate that our PtCu-SAAs are coke resistant at realistic C-H bond activation conditions as compared to bulk Pt-NPs. Combining the coke analysis with the CO-DRIFTS experiments previously described, we see that PtCu-SAAs are a stable, coke resistant catalyst with superior long term stability for these reactions.

Chapter 4 - Propane Dehydrogenation (PDH)

Following the promising C-H bond activation results in butane, we looked to extend this work to propane. Given the recent interest in propane dehydrogenation, we chose to explore this reaction with our catalyst systems and to expand the set to include PdCu-SAAs and NiCu-SAAs as well. One of the primary challenges for PDH is the strong endothermic nature of the reaction, with ΔH^0_{rxn}= 124 kJ/mol (60). This requires high temperatures to achieve useful conversions, which can quickly deactivate available catalysts through sintering and domain agglomeration as well as by coke deposition. Figure 27 below shows the equilibrium conversion for propane dehydrogenation at 1 bar, and in our system using 10% Propane, 10% H_2, and 80% He as a diluent. Operating at reduced reactor pressures and with H_2 as a diluent are common techniques employed industrially to improve yield by controlling coke formation and limiting deactivation (6) (7). These steps have competing influences on equilibrium conversion with dilution and lower partial pressures increasing conversion while the introduction of H_2 reduces K_{eq}. The following figure demonstrates the impact of the reactor conditions on the equilibrium conversion. Equilibrium conversion at 550°C in pure propane is 23%, while in our dilute system we find the maximum conversion to be 36%.

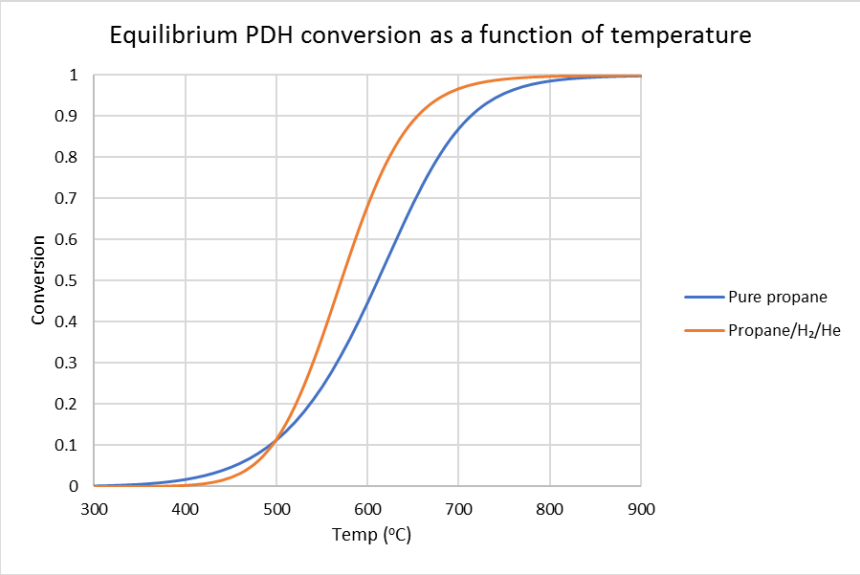

Figure 27 - Equilibrium conversion for PDH as a function of temperature for pure and dilute propane in H_2/He

CO-DRIFTS data collected from each of the spent SAA catalyst leaves it unclear whether they remain as single atom alloys at useful propane dehydrogenation temperatures. Thus, X-ray absorption techniques are needed to properly measure the dispersion and electronic environments of these materials. Despite this, kinetic measurements were made to measure the apparent activation energies of each reaction system. Additionally, deactivation studies were carried out for each system to understand the impact of the conditions on the catalyst activity.

In recent years, DFT calculations have allowed for the estimation of reaction barriers for a wide variety of C-H bond activation pathways over catalysts of interest. In a review published in 2015 by Zhao et al, a succinct table of aggregated data collected from many DFT focused publications presented the calculated C-H bond activation energy on various surfaces (31). A partial table is reproduced below to provide some insight for the activation energies for our catalyst systems. In this work, initial C-H bond activation in methane was considered.

Table 7 - Calculated activation energies for initial C-H bond activation for methane dehydrogenation on different metal surfaces. Reproduced from (32).

Surface	E_a (kJ/mol)	Software	Reference
Cu(100)	145	SIESTA	(61)
Cu(111)	171	Dmol	(62)
Cu(100)	153	Dmol	(62)
Cu(111)	151	VASP	(63)
Cu(111)	158	VASP	(63)
Cu(111)	188	VASP	(64)
Cu(211)	138	VASP	(64)
Ni(111)	126	ADF-BAND	(65)
Ni(100)	119	ADF-BAND	(65)
Ni(553)	104	ADF-BAND	(65)
Ni(111)	114	CASTEP	(66)
Pd(111)	92	CASTEP	(67)
Pt(111)	82	CASTEP	(68)
Pt(111)	90	VASP	(69)

Here, we see that initial C-H bond activation is expected to proceed much more readily over Ni, Pd, and Pt than on Cu. A simple reactivity series can be considered by comparing activation energies over the <111> face for each metal. This gives

$$Pt \sim Pd < Ni << Cu \qquad (7)$$

While considering the activation energy on metal single crystals is informative, a more complete treatment must include the electronic and geometric impact of the support material as well. Indeed, some authors have suggested that it is entirely unsuitable to consider just the catalytically active species alone without the support effects (32). For example, in the case of single atom metal catalysts, anchored metal atoms often carry some charge due to electronic effects from the support (32) (70) (71). For example, CO-DRIFTS and X-ray absorption studies on single atom Pt/FeOx catalysts reveal surface Pt atoms are partially charged, $Pt^{\delta+}$ (72). To rationalize the effects of our copper support, we present

below currently unpublished DFT calculations for the methane dehydrogenation reaction over Cu(111), PtCu(111)-SAAs, and Pt(111) from the Stamatakis group at University College London (58).

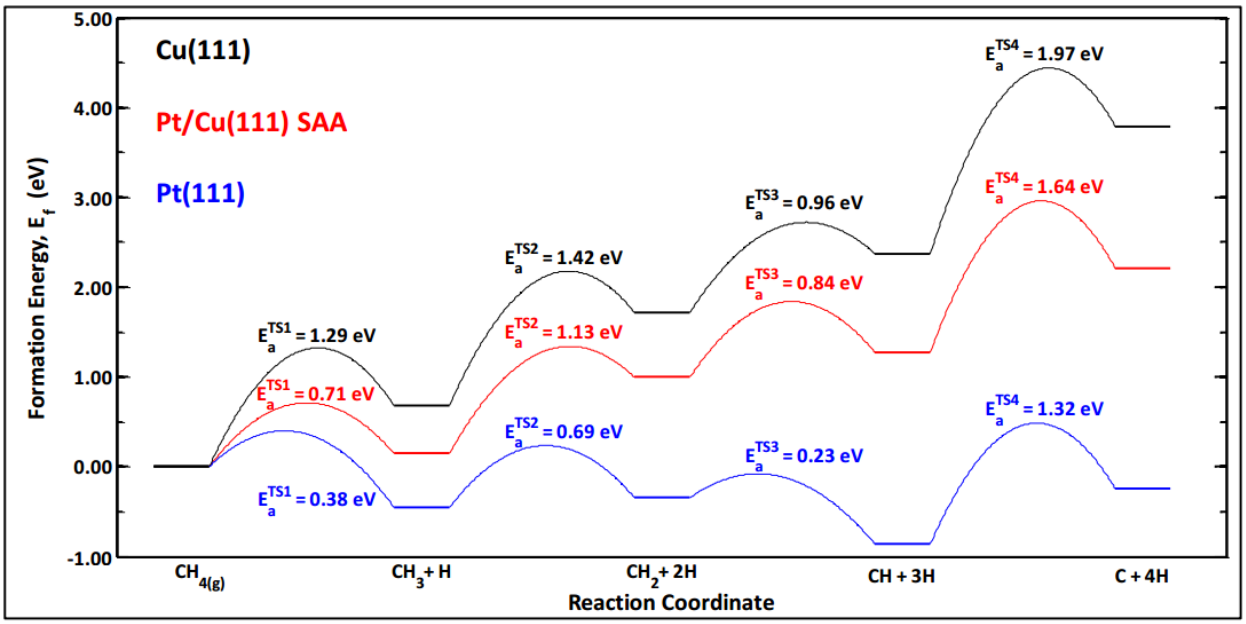

Figure 28 - DFT calculated energetics for C-H activation and binding of intermediates for methane decomposition. Unpublished data from ref (58).

Here we see much decreased activation energies for C-H bond activation on Pt(111) as compared to Cu(111), which is expected to provide significantly improved reaction kinetics. Interestingly, we see that for each dehydrogenation step, the PtCu-SAA is expected to provide intermediate activation energies *and* intermediate binding strength between the two pure metals. The activation energy change is supported by our C-H bond activation work with butane, and a careful balance of adsorption strengths has previously been identified as an important characteristic for good catalysts giving rise to the well-known volcano plots. Extension of these findings to other metals is a reasonable first approximation, and our work looks to test the hypothesis that activation energies for our single atom alloys are intermediate between the copper support and the catalytically active metal. Additionally, we seek to show that the reduction in adsorption strength produces catalysts which are more coke-resistant, due to ease of product desorption, than their monometallic equivalents.

Pd catalysts for PDH

Deactivation kinetics were examined for PdCu-SAAs and Pd-NPs. Figure 29 below shows the conversion plots for each sample during long time-on-stream experiments at 550°C.

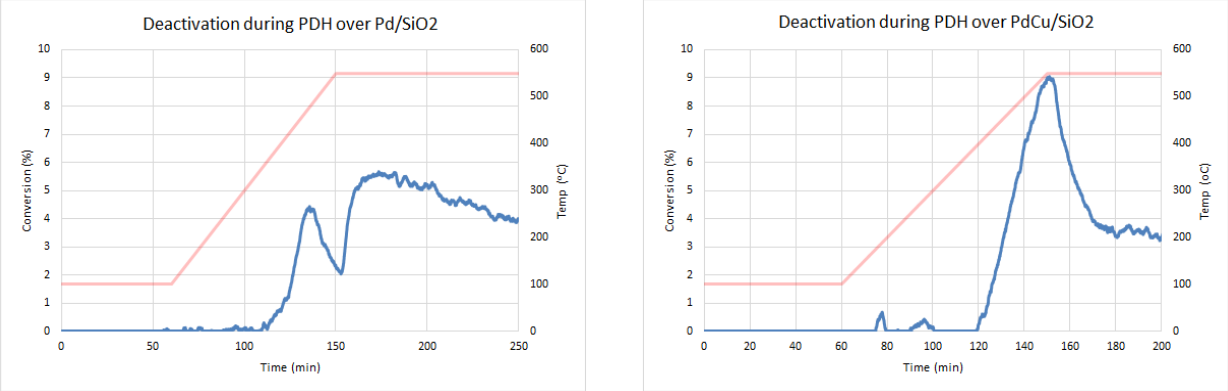

Figure 29 - Deactivation during PDH for Pd-NPs (left) and PdCu-SAAs (right). 219mg 0.5wt% Pd-NPs. 10.8% Propane/10.0% H_2/bal He, total flow rate = 22.5mL/min. 144mg $Pd_{0.01}Cu$-SAAs. 10.4% Propane/10.0% H_2/bal He, total flow rate = 23.6mL/min. Temperature ramp at 5°C/min

One interesting feature of the bulk Pd-SAAs is the onset of activity as low as 300°C, followed by rapid deactivation. As with Pt-NPs it is assumed that the low temperature activity is due to highly active dehydrogenation sites, such as step sites, with a high degree of coordinatively unsaturated Pd atoms. This is consistent with DFT calculations which show lower dehydrogenation barriers for stepped (221) surfaces as compared to terrace (111) sites in methane (64). Rapid deactivation follows, likely due to coking from over dehydrogenation. This low temperature peak is notably absent from the PdCu-SAA even after reduction at 550°C, although some small amount of low temperature-activity is noted, perhaps indicating a dimer or larger Pd ensemble content on this catalyst.

The deactivation kinetics were quantified for each catalyst system. Both first and second order deactivation kinetics were fitted based on the initial deactivation rates of the catalysts. Linear plots are presented below in Figure 30 to calculate the deactivation constant, k_d. For the Pd-NP sample, each deactivation step was measured independently. From Equation 2 we see that the slope of the first

order deactivation plot should be equal to k_d. From Equation 4, we find that the slope for second order kinetics plots is

$$k_d \left[\frac{1 - X_{A,0}}{X_{A,0}}\right]$$

Calculated values are presented in Table 11.

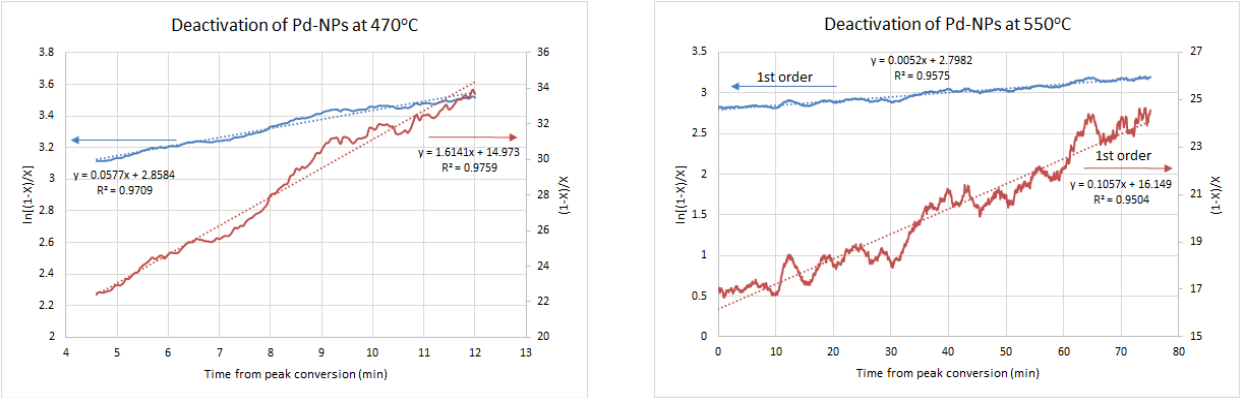

Figure 30 - Linear deactivation plots for first and second order deactivation in Pd-NPs

From the two plots above, it is clear that both deactivation models provide reasonable fits for the deactivation kinetics, which unfortunately does not allow us to discriminate between the expected first order deactivation kinetics of coking and second order kinetics of particle sintering. Figure 31 below plots both models on the actual conversion data for this catalyst.

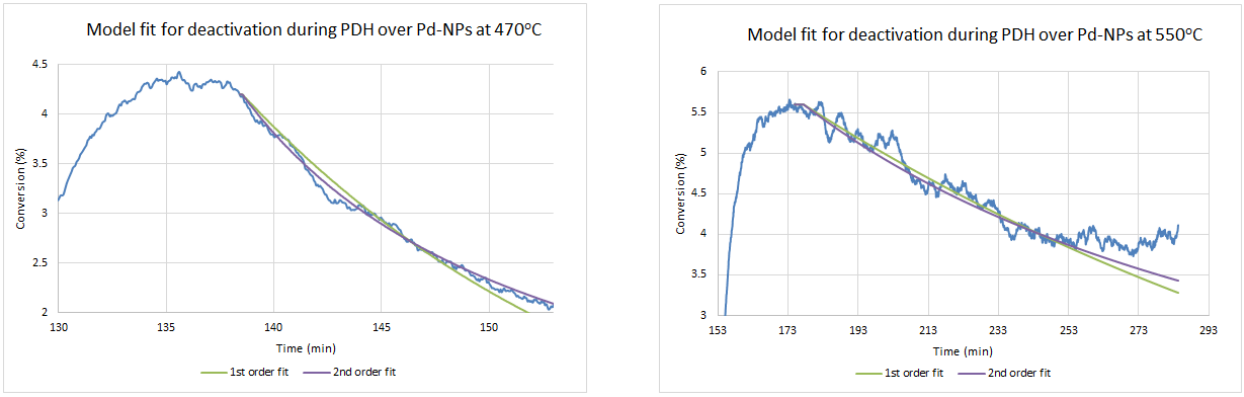

Figure 31 - Model fit for first order (green) and second order (purple) deactivation of Pd-NPs

Figure 32 below shows the same analysis for the PdCu-SAA sample.

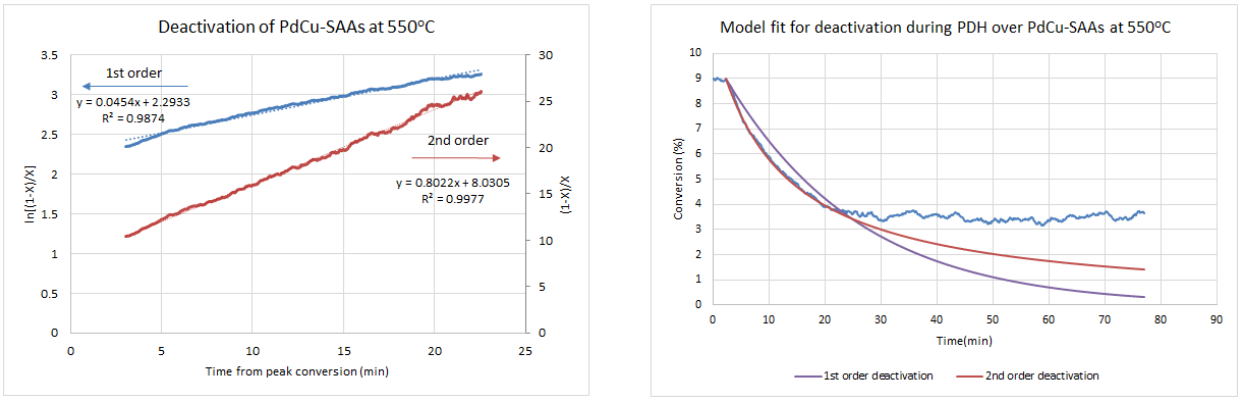

Figure 32 - Model fit for first and second order deactivation kinetics over PdCu-SAAs

Although both models show reasonable linear fit of their respective kinetic equations, the second order kinetic model is visually a better fit for the actual conversion data. TPO was performed to help differentiate between these two mechanisms. Calculated deactivation constants are presented in Table 8.

Kinetic experiments were carried out using a temperature profile with isothermal steps to allow steady state measurements of the catalyst activities for each Pd catalyst at different temperatures. Reaction rates were calculated from the mass spectrometry data in several steps. First, calibration curves for

propane and propene mole fraction were generated using m/z=42 and 44 mass spec data. For kinetic experiments, conversion was calculated as $X_{propene}/X_{propane,0}$ where X_i is the mole fraction of species i. These values were used to calculate the reaction rate using the differential form of the PBR mole balance.

$$\frac{dX}{dW} = -\frac{r'_A}{F_{A,0}}$$

$$\int_0^X dX = \int_0^W -\frac{r'_A}{F_{A,0}} dW$$

$$-r'_A = \frac{XF_{A,0}}{W}$$

Where $-r'_A$ is the reaction rate for propene formation with units $\frac{mol}{sec*g_{cat}}$, W is the catalyst weight, $F_{A,0}$ is the initial flow rate of propane, and X is the mole fraction of propene in the effluent stream. In the cases of the monometallic NP catalysts, correlations were used to estimate the amount of metal available at the catalyst surface. Boucher el al. showed that monometallic Pd-NPs prepared by IWI are well dispersed, with diameter ≈ 2nm for metal loadings as high as 4.8 atom% (20wt%) (29). Using this value as a reasonable approximation for monometallic nanoparticle diameters in this study, correlations presented by Smith and Notheisz were used to estimate the fraction of exposed atoms. In their work, Smith and Notheisz show that experimental values for the fraction of exposed metal atoms derived from chemisorption experiments agree well with a simple 1/d relationship (73). That is,

$$Fraction\ exposed\ (FE) = \frac{1}{metal\ crystallite\ diameter\ in\ nm}$$

With a 2nm average particle diameter, this gives FE = 50%. As a result, all of the reaction rates presented below for monometallic NPS are calculated assuming only half of the catalytically active metal participates in the reaction. For SAA catalysts, it is assumed that all of the noble metal atoms are

available as catalytic sites. For kinetic calculations, this provides a reasonable lower bound for the activity of the single atom alloys. Additional particle characterization is required to measure the surface Pt, Pd, or Ni concentration in the SAAs to make a more definitive calculation.

Figure 33 below shows the reaction rate plots for Pd-NPs and PdCu-SAAs as a function of reaction temperature.

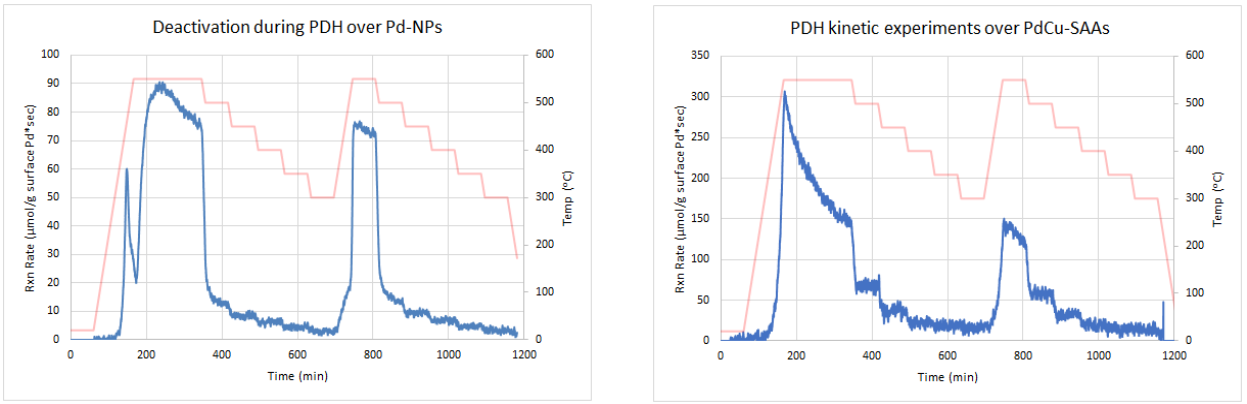

Figure 33 – Rate measurements for the PDH reaction over Pd Catalysts. 110mg 5wt% Pd-NPs. 13.1% Propane/9.5% H_2/bal He, total flow rate = 62.37mL/min. 214mg $Pd_{0.01}Cu$-SAAs. 9.9% Propane/10.0% H_2/bal He, total flow rate = 61.8mL/min. Temperature ramp at 5°C/min

When normalized to the estimated number of Pd atoms available at the surface, the reaction rates are much higher for the PdCu-SAA samples than the Pd-NPs. This is an indication that surface coke on the monometallic NPs is reducing the number of active sites available for the reaction. Additional catalyst characterization, such as quantitative chemisorption to measure active surface area in Pd-NPs, would be required to calculate turnover frequency for a direct comparison on an atom basis. One interesting observation for these materials is that in both cases, reaction at 550°C causes rapid deactivation, while the second cycle data returns to roughly the same activity upon heating to the same temperature. This indicates that little deactivation takes place at 500°C and below, and we may be operating near the "light-off" temperature for coke formation.

Using the reaction rate data presented above, the average rate was calculated for each steady state temperature regime. Figure 34 below shows the Arrhenius-type plots generated from this rate data.

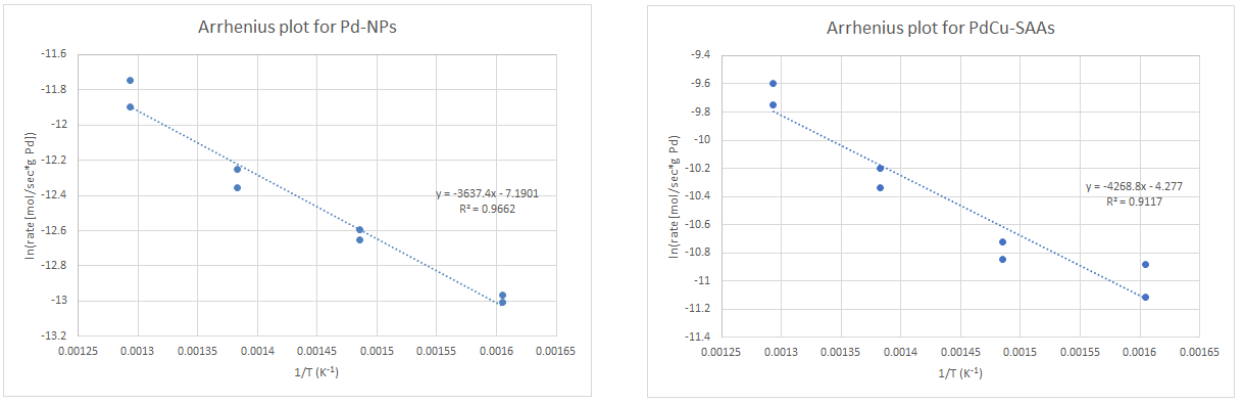

Figure 34 - Arrhenius plots for Pd-NPs (left) and PdCu-SAAs (right)

Since the slope of the Arrhenius plot is $-E_{app}/R$, we can calculate the apparent activation energy for each catalyst. The uncertainty in the activation energy is taken to be the standard error calculated from the least squares regression in the Arrhenius plot. Tabulated values for E_{app} are presented in Table 8.

Comparison of the reaction rates measured in the ascending temperature regime allows for calculation of E_{app} in a regime that is potentially unencumbered by coke formation. Using the data presented in Figure 29, Arrhenius-type plots were generated for each sample.

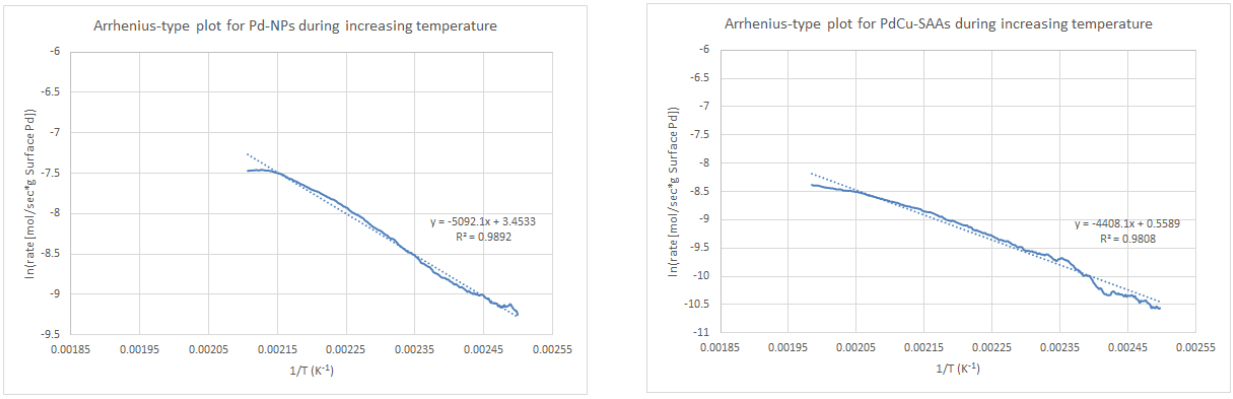

Figure 35 - Arrhenius-type plots for the ascending temperature regime in Pd-NP and PdCu-SAAs.

Tabulated values for E_{app} are presented in Table 8.

To evaluate the coke generation on each sample, temperature programmed oxidation (TPO) was carried out. The samples were first pretreated at 300°C to remove volatile organic compounds. Next, they were heated to 600°C at 3°C/min in 10% O_2/He and CO_2 generation was monitored by mass spectrometry. Figure 36 presents this data normalized by the catalyst surface metal loading as before. Note that the PdCu-SAA signal is presented at 10x to make it visible on the plot.

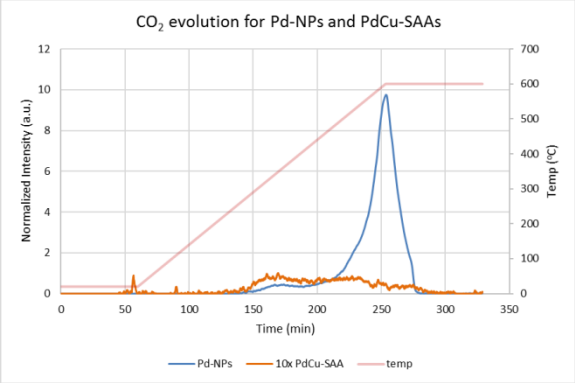

Figure 36 – TPO data for Pd-NPs and PdCu-SAAs. Note that the PdCu-SAA data is presented at 10x magnification. 100mg spent catalyst. Sample purged in Argon at 300°C followed by heating from room temperature to 600°C at 3°C/min using 20% O_2 in Ar, total flow = 50mL/min.

Two distinct CO_2 evolution peaks are noted, with the low temperature peak corresponding to CO_2 evolution from support effects as observed in Figure 26. The higher temperature peak can be used to judge the extent of coke domain growth and graphitization since lighter coke (smaller degree of graphitization) will be more susceptible to lower temperature oxidation (74). In addition to negligible coke deposition on the SAA catalyst, we see a shift to lower temperatures indicating smaller, less graphitized domains. Indeed, this CO_2 evolution is consistent with that seen on the silica support in the C-H bond activation experiments with butane. CO_2 evolution peaks were integrated, and the resulting total coke content is presented in Table 8.

Table 8 – Data summary for Pd-NPs and PdCu-SAAs

		$k_d x10^3$ at 470°C	$k_d x10^3$ at 550°C	E_{app} increasing temp	E_{app} decreasing temp	Coke formation
	Catalyst	(min^{-1})	(min^{-1})	(kJ/mol)	(kJ/mol)	g C/g metal
First order	Pd-NP	58	5	42±1	30±2	12.28
	PdCu-SAA	-	45	37±1	35±5	0.37
Second order	Pd-NP	73	6			
	PdCu-SAA	-	79			

Given comparable deactivation kinetics between samples and much lower coke deposition on the SAA catalysts, PdCu-SAA deactivation is attributed primarily to particle sintering or Pd diffusion into the subsurface. Pd migration would be consistent with the high surface energy of elemental Pd compared to Cu (75), though the presence of hydrogen and butane in the reaction system may change this picture. There is a small reduction in E_{app} between the ascending temperature measurements, and those made in the descending temperature regime following deactivation. This reduction in E_{app} is consistent with catalyst deactivation by coking or pore closure leading to diffusion limitations within the system with the apparent activation energy for strongly diffusion limited systems is expected to approach $E_a/2$ (18) (20). Reduction in E_{app} by 12kJ/mol for the monometallic Pd and only 2kJ/mol for the PdCu-SAAs indicates the diffusion limitations are more severe in the case of the monometallic catalyst. This is further support for our hypothesis of deactivation primarily by particle sintering or subsurface metal diffusion in the PdCu-SAAs. Additional characterization is needed to determine the final state of these catalysts after exposure to the temperature and reagents specific to PDH reactions. XPS could be used to characterize the surface composition since high resolution STM will be challenging here due to the similar z-number of Pd and Cu.

Pt catalysts for PDH

Similar long time-on-stream experiments were carried out for Pt-NPs and $Pt_{0.03}Cu$-SAAs. The reaction conditions were the same as those used for Pd catalysts.

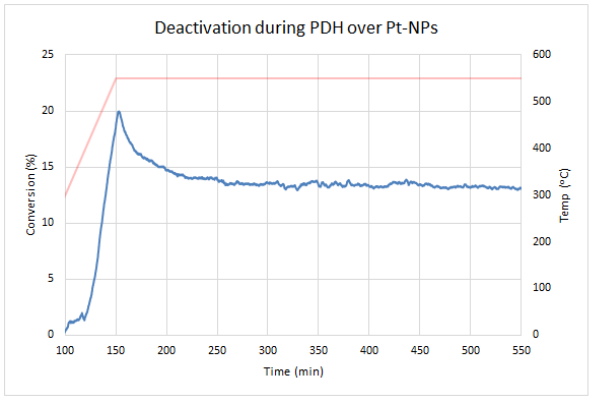

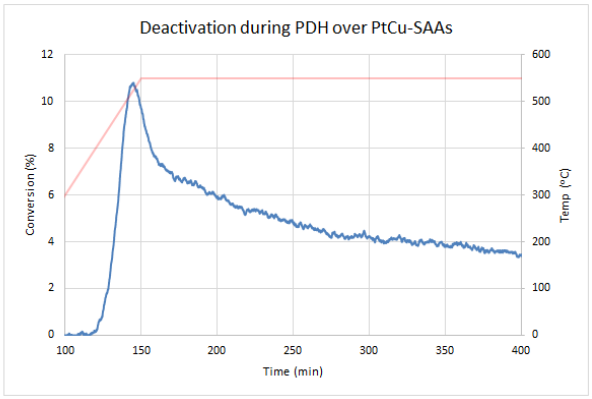

Figure 37 - Deactivation during PDH for Pt-NPs (left) and PtCu-SAAs (right). 55mg 0.5wt% Pt-NPs. 10.3% Propane/9.7% H_2/bal He, total flow rate = 25.3mL/min. 205mg $Pt_{0.01}Cu$-SAAs. 9.9% Propane/8.5% H_2/bal He, total flow rate = 23.7mL/min. Temperature ramp at 5°C/min

k_d was calculated for each sample and deactivation model from the appropriate conversion equation listed previously and the plots below. Calculated k_d values are presented in Table 9.

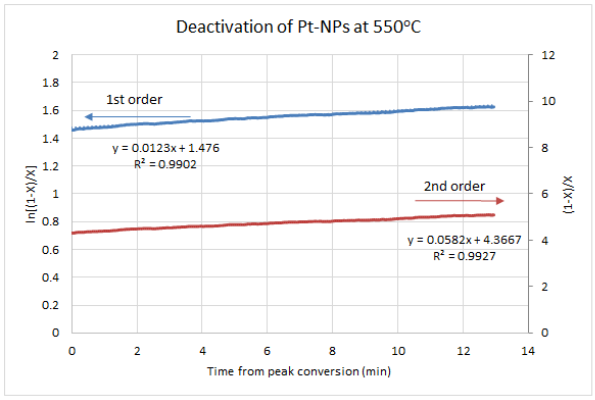

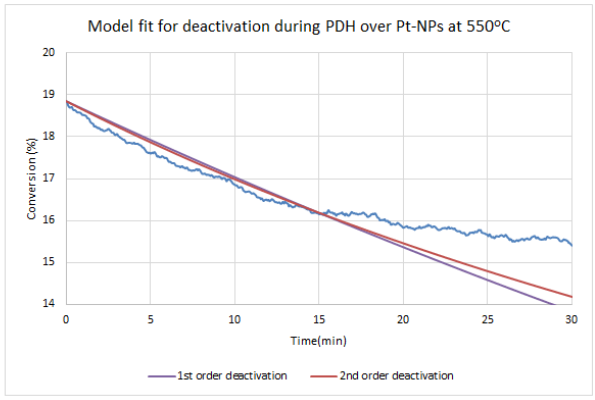

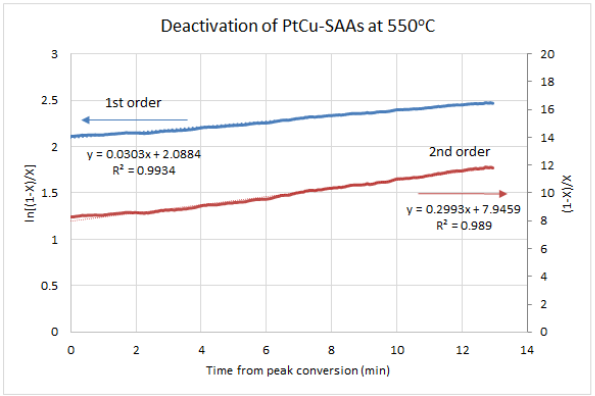

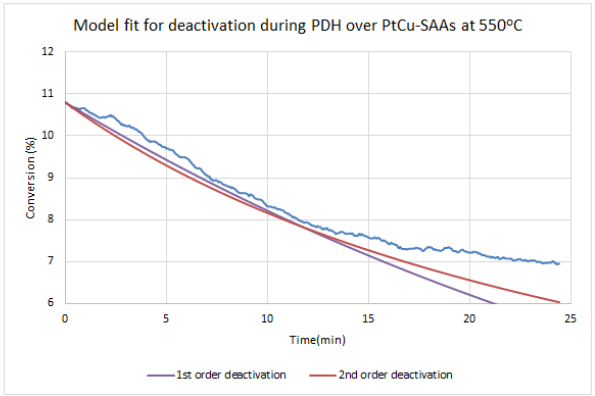

Figure 38 - Model fit for first and second order deactivation kinetics over Pt-NPs (top) and PtCu-SAAs (bottom)

E_{app} was also calculated as before during the increasing temperature, non-isothermal reaction steps.

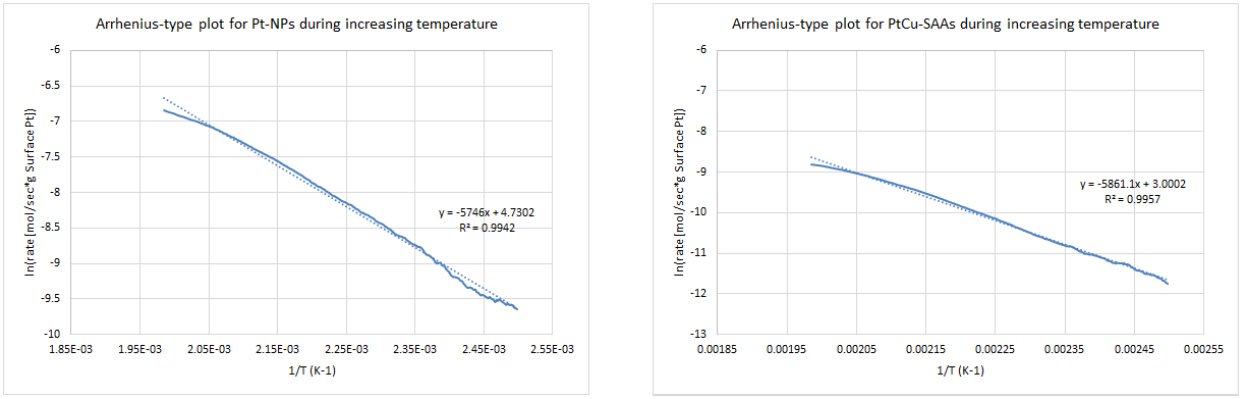

Figure 39 - Arrhenius-type plots for the ascending temperature regime in Pt-NP and PtCu-SAAs

As with Pd containing particles, kinetic experiments were carried out for Pt-NPs and PtCu-SAAs.

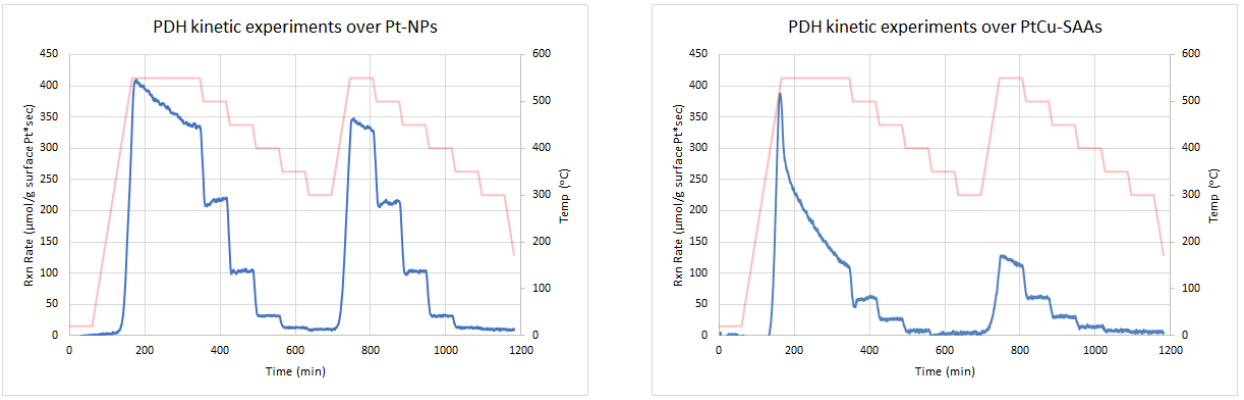

Figure 40 - PDH kinetics over Pt catalysts. 96mg 0.5wt% Pt-NPs. 12.5% Propane/10.0% H_2/bal He, total flow rate = 60mL/min. 220mg $Pt_{0.01}Cu$-NPs. 10.3% Propane/9.6% H_2/bal He, total flow rate = 62mL/min. Temperature ramp at 5°C/min

Here we find that the absolute rate for PtCu-SAAs normalized as before to the estimated surface Pt area is lower than the Pt-NP sample, which is in line with the expected activity discussed previously based on DFT calculations and the copper support effects. Calculation of the activation energy for these samples (Table 9) shows lower activation energy on the SAAs, though the two values are not statistically different.

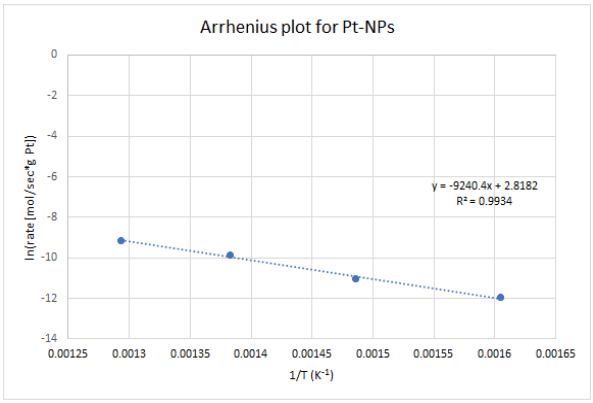

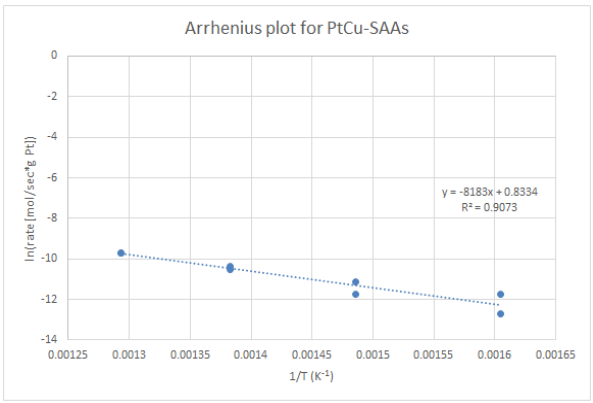

Figure 41 – Arrhenius-type plots for Pt-NPs (left) and PtCu-SAAs (right)

Using the reaction rate data measured for PtCu- and PdCu-SAAs, we can plot them on the same axes to define the temperature regimes for which each catalyst is expected to provide better activity.

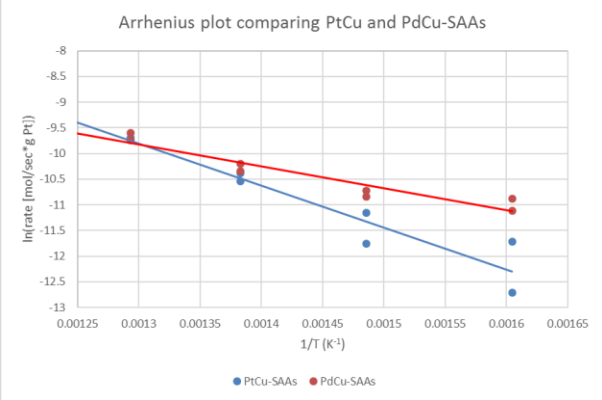

Figure 42 - Comparison of activity for PtCu- and PdCu-SAAs

Here, we see that for $\frac{1}{T} < 1.306 * 10^{-3}$, that is, T=493°C, the PdCu-SAAs show higher activity than the PtCu-SAAs due to their different apparent activation energies. However, more detailed kinetic tests should be repeated at low temperatures in the absence of carbon fouling to ensure that the low E_{app} values calculated here are not masked by the intrusion of pore- diffusion limitations.

TPO data for Pt-NPs and PtCu-SAAs are presented in the following plot.

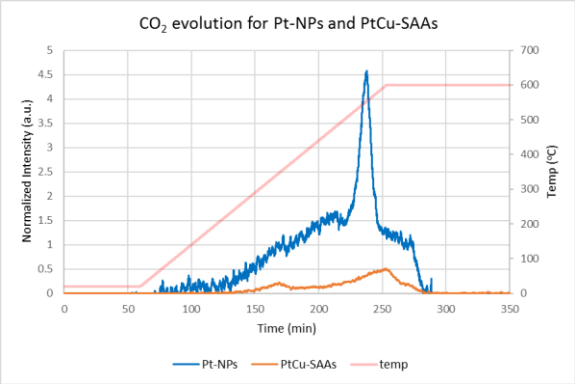

Figure 43 - TPO data for Pt-NPs and PtCu-SAAs. 100mg spent catalyst. Sample purged in Argon at 300°C followed by heating from room temperature to 600°C at 3°C/min using 20% O_2 in Ar, total flow = 50mL/min.

Again, we see two distinct CO_2 evolution peaks. The onset of coke oxidation is similar for both samples. We see much lower levels of coke deposition on the single atom alloy when normalized for the estimated surface Pt, as was the case previous samples. This indicates that the SAA is more coke resistant than the corresponding monometallic nanoparticles. Given the higher rate of deactivation on PtCu-SAAs but lower coke formation, we again attribute the deactivation primarily to particle sintering or Pt diffusion into the subsurface Cu lattice. This can be differentiated by surface characterization, proposed for future work.

Table 9 - Data summary for Pt-NPs and PtCu-SAAs

	$k_d x10^3$ at 550°C	**E_{app} increasing temp**	**E_{app} decreasing temp**	**Coke formation**
Catalyst	(min^{-1})	(kJ/mol)	(kJ/mol)	g C/g metal
Pt-NP	12	48±1	77±3	2.50
PtCu-SAA	30	49±1	68±9	0.13

Interestingly, we see a lower E_{app} for these catalysts in the ascending temperature region. This is an important difference between the Pd catalysts, and may indicate the loss of sites which undergo facile C-H bond activation due to coking or subsurface diffusion. Additional catalyst characterization is needed

to measure the remaining Pt atoms on the surface of each catalyst after reaction to confirm this hypothesis.

Ni catalysts for PDH

The NiCu-SAA and Ni-NP systems presented significant issues during the course of the work. Noisy baselines and very low conversions prevented the collection of good deactivation and kinetic data. It is possible that excessive coke formation at low temperatures accounts for some of the low activity, but Kang et al report severe reduction in hydrogenation of butadiene associated with nickel catalysts by alloying with copper (53). They attribute this loss in activity to differences in lattice parameters and lower surface energy for copper compared to nickel leading to segregation, which tends to drive nickel subsurface (53). The resulting surface is copper-rich, with a separate subsurface nickel-rich phase. However, it has also been demonstrated that the final catalyst composition is dependent on the reaction atmosphere. Nerlov et al. showed that high gas phase CO concentrations can influence the surface composition in Ni/Cu bimetallics by strongly binding the Ni atoms making their migration thermodynamically unfavorable (76). It is possible that the reducing atmosphere containing propane will be enough to keep the Ni atoms at the surface layer by providing adsorbed groups to prevent and dissolution. Indeed, good signal intensity by CO-DRIFTS for the NiCu-SAAs indicates a relatively high surface Ni population.

Despite noisy background data, plots for deactivation kinetics calculations are presented in Figure 44 below.

Figure 44 – Deactivation kinetics data for Ni-NP and NiCu-SAAs. A and B show raw conversion data. k_d measurements and deactivation model fits for Ni-NPs (C, D) and NiCu-SAAs (E, F) are also shown. Conditions for A, C, E - 209mg 0.1 wt% Ni-NPs. 9.7% Propane/9.3% H_2/bal He, total flow rate = 24.6mL/min. Conditions for B,D,F - 309mg $Ni_{0.005}Cu$. 12.9% Propane/9.8% H_2/bal He, total flow rate = 62.2mL/min. Temperature ramp at 5°C/min

Again, we see reasonable fits for first and second order deactivation in both samples. Calculated deactivation constants are reported in Table 10 below.

Kinetic experiments for Ni-NPs and NiCu-SAAs were carried out with mixed results. Due to insufficient signal to noise ratio for the 0.1 wt% Ni-NP sample for kinetic calculations a new sample was prepared

with 1.8 wt% Ni on silica. This sample was used for the PDH kinetic experiments, but over-dehydrogenation led to almost complete consumption of propane and propene in the sample and no activity above the baseline indicating a complete deactivation surface due to coke formation. Because of this, the activation energy could not be calculated.

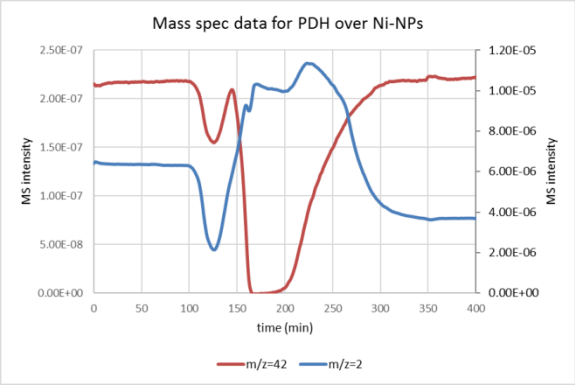

Figure 45 - Severe coke formation and deactivation noted on Ni-NPs. 132mg 1.8% Ni-NPs. 10.7% Propane/9.3% H_2/bal He, total flow rate = 61.5mL/min. Temperature ramp at 5°C/min.

For the NiCu-SAA sample, kinetic data is presented below.

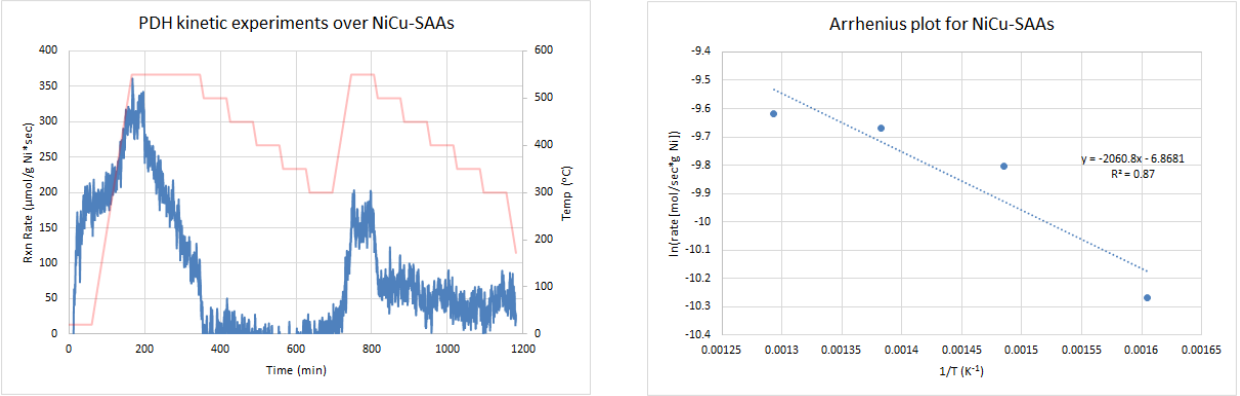

Figure 46 - PDH kinetics over NiCu-SAA. 309mg $Ni_{0.005}Cu$. 12.9% Propane/9.8% H_2/bal He, total flow rate = 62.2mL/min. Temperature ramp at 5°C/min.

Due again to extremely low activities for our NiCu catalysts for PDH, there is considerable noise in the data. Reaction rate data was used only for second cycle in this case for activation energy calculations.

The calculated E_{app} value is presented in Table 10. TPO for the long time-on-stream samples is presented below in Figure 47.

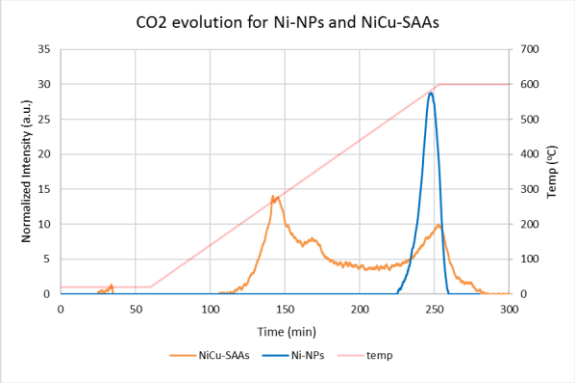

Figure 47 - TPO data for Ni-NPs and NiCu-SAAs. 100mg spent catalyst. Sample purged in Argon at 300°C followed by heating from room temperature to 600°C at 3°C/min using 20% O_2 in Ar, total flow = 50mL/min.

Interestingly, the NiCu-SAA catalyst shows more total carbon deposition than the Ni-NP samples, with two obvious peaks. The high temperature peaks in this case correspond to graphitic coke, while the low temperature peak is consistent with oxidation of adsorbed hydrocarbons. Despite the desorption step carried out at 300°C, some hydrocarbon material may have remained on this catalyst. Deactivation of both Ni-NPs and NiCu-SAAs is more consistent with activity loss due to coking in contrast to the Pt, Pd samples. Calculated coke production normalized for metal content is presented in Table 10.

Table 10 -Data summary for Ni-NPs and NiCu-SAAs

	$k_d x10^3$ at 550°C	**E_{app} increasing temp**	**E_{app} decreasing temp**	**Coke formation**
Catalyst	(min^{-1})	(kJ/mol)	(kJ/mol)	g C/g metal
Ni-NP	29	-	-	3.22
NiCu-SAA	7	-	17±5	4.04

Chapter 5 – Summary and Conclusions

Single atom platinum, palladium and nickel supported in copper nanoparticle surfaces were prepared for use in C-H bond activation experiments and were explored as potential PDH catalysts. These bimetallic systems were chosen based on available DFT calculations indicating that they should provide coke-resistant surfaces capable of facile C-H bond activation. In our studies, the PtCu- and PdCu-SAAs showed superior coke resistance when compared to monometallic Pt and Pd nanoparticles under realistic propane dehydrogenation conditions and the PtCu-SAA system showed similar results for C-H bond activation in butane. The available data from our deactivation kinetics experiments is most consistent with deactivation by particle sintering and migration of Pt and Pd subsurface in SAA catalysts, while the NiCu system is more consistent with deactivation by coking. Additionally, the apparent activation energy for each catalyst was calculated using isothermal steady state experiments under PDH conditions. Experimental data for the deactivation rate measurements, kinetic experiments, and coke analysis are presented in Table 11.

Table 11 – Data summary for SAAs and NPs

		$k_d x10^3$ at 470°C	$k_d x10^3$ at 550°C	E_{app}, increasing T	E_{app}, decreasing T	Coke formation
	Catalyst	(min^{-1})	(min^{-1})	(kJ/mol)	(kJ/mol)	g C/g metal
First order	Pd-NP	58	5	42±1	30±2	12.28
	PdCu-SAA	-	45	37±1	35±5	0.37
	Pt-NP	-	12	48±1	77±3	2.50
	PtCu-SAA	-	30	49±1	68±9	0.13
	Ni-NP	-	29	-	-	3.22
	NiCu-SAA	-	7	-	17±5	4.04
Second order	Pd-NP	73	6			
	PdCu-SAA	-	79			
	Pt-NP	-	14			
	PtCu-SAA	-	36			
	Ni-NP	-	39			
	NiCu-SAA	-	10			

As both first and second order deactivation fit the available data well, we will consider here the first order deactivation constants for comparison. In the case of Pd-NPs, the low temperature deactivation makes it difficult to compare directly to PdCu-SAAs, but a simple comparison can be made simply by adding the two constants together. This leads to the following comparison of deactivation rates, which is likely a combination of sintering and coke deposition effects.

$$\text{NiCu-SAAs} < \text{Pt-NPs} < \text{Ni-NPs} \approx \text{PtCu-SAAs} < \text{PdCu-SAAs} < \text{Pd-NPs} \quad (8)$$

Lowest deactivation ---------- Highest deactivation

In the case of the SAA catalysts, it is hypothesized that activity loss in PtCu-SAAs and PdCu-SAAs is consistent with particle sintering, while NiCu-SAA is attributed primarily to coking. Coking and pore closure could also lead to significant diffusional barriers, though direct evidence of a reduction in activation energy attributed to this phenomenon is limited to the Pd-NP and PdCu-SAA systems. Additionally, there is no change in E_{app} for first and second cycle kinetic experiments indicating that the

diffusional barriers introduced by coke deposition and pore closure are rapid and are largely realized during the initial heating to 550^{o}C. Thus, it is believed that the monometallic NP samples are more consistent with deactivation by coking, though additional characterization for all samples is needed to confirm these claims. These results are consistent with butane C-H bond activation results, showing low coke formation on PtCu-SAAs, and expected behavior over Ni catalysts (58) (53).

With the exception of the Pt system, we see the expected behavior that the single atom alloy shows superior stability compared to their monometallic nanoparticle counterparts. That is, we see k_d for Pd-NPs>PdCu-SAAs, and k_d for Ni-NPs>NiCu-SAAs while the opposite is true for the Pt/PtCu catalysts. It should be noted that due to the very low conversion and high signal to noise ratios for the NiCu-SAA system, there is considerable uncertainty in these measurements which is not well captured by standard regression techniques.

Coke analysis of the catalyst samples used in this study show the following normalized coke deposition propensities:

Pd-NPs>NiCu-SAAs>Ni-NPs>Pt-NPs>PdCu-SAAs>PtCu-SAAs (9)

Most coke ---------- Least coke

This trend generally confirms that single atom alloys show superior coke resistance to traditional monometallic catalysts. The PtCu system shows much less coke deposition than other catalysts in this series, which is consistent with the butane C-H activation work and supports our hypothesis that the copper surface allows for the coupling and desorption of coke precursors from the catalyst surface.

Activation energy calculations at approximate steady state conditions following coke deposition at 550^{o}C for each catalyst system generally shows no statistical difference between SAA and monometallic NP catalyst, and activity trends among metals are as expected.

$$\text{Pt-NPs} \approx \text{Pt-SAAs} > \text{Pd-NPs} \approx \text{PdCu-SAAs} > \text{NiCu-SAAs} \quad (10)$$

Highest E_{app} ---------- Lowest E_{app}

Additional replicates are needed to determine if the activation energy for these systems is in fact statistically different. Examining the values calculated for each catalyst system leads to a few interesting conclusions. First, the Pt-NP and PtCu-SAA catalysts are generally near the values expected based on the available DFT literature presented previously. Interestingly, we see similar values for the monometallic and SAA catalysts, despite expecting the activation energy for the single atom alloy system to be somewhat higher. One interpretation of this is that aggregation of isolated Pt atoms on the catalyst surface has created a catalyst where the active sites are actually extended Pt ensembles, such as islands or chains. However, if the resulting catalyst can be shown to still be single atom, this is an exciting finding. This would imply a coke resistant catalyst where we don't pay the energetic penalty expected by creation of the bimetallic.

In the Pd-NP and PdCu-SAA catalyst we find that the activation energy is lower than expected based solely on the base metal energetics. Coupled with the low coke propensity found on the PdCu-SAA sample, this makes the PdCu-SAA system an important catalyst for additional exploration. Examining the reaction rate of these two catalysts in our kinetic experiments we find that the normalized reaction rate is higher in the case of the PdCu-SAA for $T<493^{o}C$. Based on the calculated coke deposition values, this implies that the coke resistant PdCu system could have significantly improved activity in long term installations compared to Pd-NPs. The early activation and loss in activity accompanied by a decrease in E_{app} observed in the Pd-NP kinetic experiments is consistent with the early development of surface coke which would obstruct active sites and lower overall reaction rate. Of note, the absolute reaction rate in the case of PdCu-SAAs is higher than that of the PtCu-SAA system for temperatures less than about $500^{o}C$.

Conclusions

PtCu, PdCu, and NiCu-SAAs were explored for C-H bond activation using butane and propane and were compared to their monometallic nanoparticle equivalents. The propane work took place in realistic propane dehydrogenation conditions, which are expected to remain industrially relevant due to the increase in shale gas production in the US. It was found that in both reactions, addition of catalytically active metals to the copper surface greatly increases the reaction rate. PtCu-SAAs showed superior coke resistance to other lab made catalyst for C-H bond activation and PDH, while the PdCu-SAA system showed the highest normalized reaction rate. PDH reactions also showed improved coke resistance for PdCu-SAAs, while NiCu-SAAs showed increased coke deposition compared to Ni-NPs making PdCu-SAAs attractive catalysts for addition work.

Chapter 6 – Recommendations for future work

Additional work is needed to characterize the spent catalysts to fully understand the impact of the reaction conditions on the single atom alloy catalysts. After establishing long term stability for PtCu-SAAs at 360^{o}C, while all catalysts showed some signs of aggregation after exposure to 550^{o}C, future studies are needed to better define the stable operating envelope for these catalysts. Based on the analysis of our kinetic experiments, the PdCu-SAA system appears the most promising for low temperature applications having a reaction rate higher than that of the PtCu-SAA system. Given our findings that under realistic working conditions at T<~500^{o}C the PdCu-SAA system shows superior reaction rates to the other catalysts tested, this should be the focus of future work on this topic.

While exploring lower temperature regimes with each catalyst system, it is recommended to measure reaction rates and to generate Arrhenius-type plots for kinetic experiments made in ascending temperature order, and over a more narrow temperature range to limit changes in coke deposition rates due to temperature. This would allow for the comparison of apparent activation energies in a

relatively coke-free system. These comparisons will be useful in deconvoluting the contributions of diffusion barriers and changes in rate determining steps, which may accompany increasing coke formation on the particle surface. Full kinetic investigations, including reaction rate orders, are also recommended to identify correlations of catalyst reactivity to its structure/chemical composition.

Surface characterization and comparison between catalyst systems would provide an especially interesting data set to observe the possible effects of coke deposition, such as selective deactivation of highly active sites in each catalyst. To this end, it would be prudent to carry out a more detailed coke analysis study to compare the coke deposition at each steady state temperature regime to define a more stable operating envelope. Several equipment improvements may be required to measure low conversions at reduced temperatures and find ideal operating ranges for each catalyst. Additionally, catalyst loading can be increased in the cases where conversions are low.

Based on the data collected for our catalyst systems, there is promise in the dehydrogenation of higher alkanes. Due to the reduction in C-H bond activation energy as carbon number increases, dehydrogenation of butane to butene, or butadiene, or the dehydrogenation of isobutane to isobutylene may provide more interesting model systems. For these dehydrogenation reactions, reasonable equilibrium conversions are obtainable at lower temperatures where our catalysts are more stable. A literature review should be conducted to identify industrially important target molecules where the dehydrogenation reactions may be carried out at lower temperatures.

Additionally, DFT work should be used to better refine target catalyst systems for propane dehydrogenation. If further reductions in adsorption strength are required, metals such as silver or gold with filled d-orbitals, and even lower d-band centers, should be explored as catalyst supports. Additional work is needed to identify optimal bimetallics for these reactions, followed by synthesis work, characterization, and eventual catalytic testing to determine their use as dehydrogenation catalysts. It is

our understanding that much of the DFT work has been considered recently, and we should expect theory advancements that will help guide our experimental work to appear in the literature soon.

Recently, an interesting paper was published by Hunt et al. in which the authors synthesized core/shell titanium tungsten carbide nanoparticles with a Pt monolayer. WC nanoparticles have been a difficult synthetic target due to particle sintering during carburation reactions. By using a novel silica encapsulation method, they were able to create core/shell particles resistant to sintering up to 700^{o}C. Since our data is consistent with deactivation primarily by sintering in the case of PtCu and PdCu-SAAs, it is suggested that this may be a viable route to catalysts that are both coke resistant, as demonstrated with our single atom alloys, and sintering resistant, which is a property we should seek to improve. The feasibility of using these support particles to create sintering resistant Cu shells that are capable of galvanic replacement reactions could create an interesting line of research. Alternatively, different methods of single atom deposition and stabilization could be explored. The authors were able to show a small shift in the d-band for the Pt surface on the TiWC particles, so the theoretical basis for tuning of adsorption energies and rational coke resistant catalyst design is already established (77).

Bibliography

1. **Plotkin, Jeffrey S.** The Propylene Quandary - American Chemical Society. [Online] American Chemical Society, August 8, 2016. [Cited: February 20, 2017.] https://www.acs.org/content/acs/en/pressroom/cutting-edge-chemistry/the-propylene-quandary.html
2. **Mbeychok.** Own work**.** [Online] CC BY-SA 3.0, March 3rd, 2012. [Cited: april 15th, 2017.] https://commons.wikimedia.org/w/index.php?curid=18575265.
3. **National Energy Technology Laboratory (NETL) Strategic Center for Natural Gas and Oil.** *Modern Shale Gas Development in the United States: An Update.* 2013
4. **Energy Information Administration, EIA.gov.** Spot Prices for Crude Oil and Petroleum Products. [Online] U.S Energy Information Administration. [Cited: February 20, 2017.] http://www.eia.gov/dnav/pet/pet_pri_spt_s1_m.htm.
5. **Manufacturers, American Fuel & Petrochemical.** *Shale Gas Monetization - How to get into the action.* San Antonio, TX : s.n., 2013.
6. **Jesper J. H. B. Sattler, Javier Ruiz-Martinez, Eduardo Santillan-Jimenez, and Bert M. Weckhuysen.** *Catalytic Dehydrogenation of Light Alkanes on Metals and Metal Oxides.* 2014, Chemical Reviews, Vol. 114, pp. 10613-10653
7. **Meyers, Robert A.** *Handbook of Petroleum Refining Processes, Fourth Edition.* s.l. : McGraw-Hill Education, 2016.
8. **Reisch, Marc s.** *From Coal Tar to Crafting a Wealth of Diversity*. [Online] Chemical & Engineering News, Jan 12, 2008. [Cited: Feb 27, 2017.] http://pubs.acs.org/cen/hotarticles/cenear/980112/coal.html.
9. **Meilana Dharma Putra, Saeed M. Al-Zahrani, Ahmed E. Abasaeed.** *Oxidative dehydrogenation of propane to propylene over Al2O3-supported Sr-V-Mo catalysts.* 2011, Catalysis Communications, Vol. 14, pp. 107-110.
10. **Technology Economics.** *Propylene Production via Propane Dehydrogenation, Part 2.* 2013
11. **Prof. S. David Jackson, Peter C. Stair, Lynn F. Gladden and James McGregor.** *Metal Oxide Catalysis.* s.l. : Wiley, 2009.
12. **Jibril, B. Y.** *Propane oxidative dehydrogenation over chromium oxide-based catalysts.* 2004, Applied Catalysis A: General, Vol. 264, pp. 193-202.
13. **Fenglin Liao, TszWoon Benedict Lo, and Shik Chi Edman Tsang.** *Recent Developments in Palladium-Based Bimetallic Catalysts.* 2015, ChemCatChem, Vol. 7, pp. 1998-2014.
14. **Mishan E. Blecher, Emily A. Lewis, Alex Pronschinske, Colin J.Murphy, Michael F.G.Mattera, Melissa L. Liriano, E. Charles H. Sykes.** *Squeezing and stretching Pd thin films: A high-resolution STMstudy of Pd/Au(111) and Pd/Cu(111) bimetallics.* 2016, Surface Science, Vol. 646, pp. 1-4.
15. **Xinxiang Cao, Arash Mirjalili, James Wheeler,Wentao Xie, Ben W.-L. Jang.** *Investigation of the preparation methodologies of Pd-Cu single atom alloy catalysts for selective hydrogenation of acetylene.* 2015, Front. Chem. Sci. Eng., Vol. 9, pp. 442-448.

16. **Lars C. Grabow, Britt Hvolbæk, Jens K. Nørskov.** *Understanding Trends in Catalytic Activity: The Effect of Adsorbate–Adsorbate Interactions for CO Oxidation Over Transition Metals.* 2010, Top Catal, Vol. 53, pp. 298-310.
17. **Andreas W. Hauser, Joseph Gomes, Michal Bajdich, Martin Head-Gordon and Alexis T. Bell.** *Subnanometer-sized Pt/Sn alloy cluster catalysts for the dehydrogenation of linear alkanes.* 2013, Phys. Chem. Chem. Phys, Vol. 15, pp. 20727-20734
18. **Fogler, Scott H.** *Elements of Chemical Reaction Engineering, 4th ed.* Englewood Cliffs : Prentice-Hall, 2006.
19. **José Salmones, Jin-AnWang, José A. Galicia, Gabriel Aguilar-Rios.** *H_2 reduction behaviors and catalytic performance of bimetallic tin-modified platinum catalysts for propane dehydrogenation.* 2002, Journal of Molecular Catalysis A: Chemical, Vol. 184, pp. 203-213.
20. **Levenspiel, Octave.** *The Chemical Reactor Omnibook.* Corvallis, Oregon, 2013.
21. **Farnaz Tahriri Zangeneh, Abbas Taeb, Khodayar Gholivand, Saeed Sahebdelfar.** *Kinetic study of propane dehydrogenation and catalyst deactivation over Pt-Sn/Al203 catalyst.* 2013, Journal of Energy Chemistry, Vol. 22, pp. 726-732.
22. **H.M. Swaan, V.C.H. Kroll, G.A. Martin, C. Mirodatos.** *Deactivation of supported nickel catalysts during reforming of methane by carbon dioxide.* 1994, Catalysis Today, Vol. 21, pp. 571-578.
23. **Ming-Lei Yang, Yi-An Zhu, Chen Fan, Zhi-Jun Sui, De Chenb and Xing-Gui Zhou.** *DFT study of propane dehydrogenation on Pt catalyst: effects of step sites.* 2011, Phys. Chem. Chem. Phys., Vol. 13, pp. 3257-3267.
24. **Haibo Zhu, Dalaver H. Anjum, Qingxiao Wang, Edy Abou-Hamad, Lyndon Emsley, Hailin Dong, Paco Laveille, Lidong Li, Akshaya K. Samal, Jean-Marie Basset.** *Sn surface-enriched Pt–Sn bimetallic nanoparticles as a selective and stable catalyst for propane dehydrogenation.* 2014, Journal of Catalysis, Vol. 320, pp. 52-62.
25. **Jurka Batista, Albin Pintar, Djordje Mandrino, Monika Jenko, Vincent Martin.** *XPS and TPR examinations of gamma-alumina-supported Pd-Cu catalysts.* 2001, Applied Catalysis A, Vol. 206, pp. 113-124.
26. **Felicia Lucci, Jilei Liu, Matthew Marcinkowski, Ming Yang, Maria Flytzani-Stephanopoulos, Charles E.H. Sykes.** *Selective hydrogenation of 1,3 butadiene on platinum copper alloys at the single atom limit.* 2015, Nat. Commun., Vol. 6.
27. **Junjun Shan, Nare Janvelyan, Hang Li, Jilei Liu, Tobias M. Egle, Jianchao Ye, Monika M. Biener, Juergen Biener, Cynthia M. Friend, Maria Flytzani-Stephanopoulos.** *Selective non-oxidative Dehydrogenation of Ethanol to Acetaldehyde and Hydrogen on Highly Dilute NiCu alloys.* 2016, Appl. Catal. B: Environ., Vol. 205, pp. 541-550.
28. **Qing Li, Zhijun Sui, Xinggui Zhou, Yian Zhu, Jinghong Zhou, De Chen.** *Coke Formation on Pt–Sn/Al2O3 Catalyst in Propane Dehydrogenation: Coke Characterization and Kinetic Study.* 2011, Top Catal, Vol. 54, pp. 888-896
29. **Matthew B. Boucher, Branko Zugic, George Cladaras, James Kammert,Matthew D. Marcinkowski, Timothy J. Lawton, E. Charles H. Sykes and Maria Flytzani-Stephanopoulos.** *Single atom alloy surface analogs in Pd0.18Cu15 nanoparticles for selective hydrogenation reactions.* 2013, Phys. Chem. Chem. Phys, Vol. 15, pp. 12187-12196.

30. **Radcliffe, Charles.** *The FCC unit as a propylene source.* [Online] Intercat (Johnson Matthey), July 2007. [Cited: April 18th, 2016.] http://www.digitalrefining.com/article/1000312#.WPana4jyuUk
31. **Zhi-Jian Zhao, Cheng-chau Chiu and Jinlong Gong.** *Molecular understandings on the activation of light hydrocarbons over heterogeneous catalysts.* 2015, Chem. Sci., Vol. 6, pp. 4403-4425.
32. **Xiao-Feng Yang, Aiqin Wang, Botao Qiao, Jun Li, Jingyue Liu, And Tao Zhang.** *Single-Atom Catalysts: A New Frontier in Heterogeneous Catalysis.* 8, 2013, Accounts of Chemical Research, Vol. 46, pp. 1740-1748.
33. **Flytzani-Stephanopoulos M, Gates BC.** *Atomically dispersed supported metal catalysts.* Annu Rev Chem Biomol Eng., 2012, Vol. 3, pp. 545-574.
34. **Flytzani-Stephanopoulos, Maria.** *Gold Atoms Stabilized on Various Supports Catalyze the Water–Gas Shift Reaction.* 2014, Vol. 47, pp. 783-792.
35. **Ming Yang, Sha Li, Yuan Wang, Jeffrey A. Herron, Ye Xu, Lawrence F. Allard, Sungsik Lee, Jun Huang, Manos Mavrikakis, Maria Flytzani-Stephanopoulos.** *Catalytically active Au-O(OH)x-species stabilized by alkali ions on zeolites and mesoporous oxides.* Science, 2014, Vol. 346, pp. 1498-1501.
36. **Vanharde, R. and Hartog, F.** *Statistics of surface atoms and surface sites on metal crystals.* 1969, Surf. Sci., Vol. 15, pp. 189-230.
37. **N. Lopez, T.V.W. Janssens, B.S. Clausen, Y. Xu, M. Mavrikakis, T. Bligaard, and J.K. Nørskov.** *On the origin of the catalytic activity of gold nanoparticles for low-temperature CO oxidation.* 2004, J. Catal., Vol. 223, pp. 232-235.
38. **Jun Li, Xi Li, Hua-Jin Zhai, Lai-Sheng Wang.** *Au_{20}: A tetrahedral cluster.* 2003, Science, Vol. 299, pp. 864-867.
39. **Yoon B, Häkkinen H, Landman U, Wörz AS, Antonietti JM, Abbet S, Judai K, Heiz U.** *Charging effects on bonding and catalyzed oxidation of CO on Au8 clusters on MgO.* 2005, Science, Vol. 307, pp. 403-407.
40. **Seijiro Matsubara, Keisuke Asano, Yuichi Kajita, Mitsuru Yamamoto.** *C–H Bond Activation by Water on a Palladium or Platinum Metal Surface.* 2007, Synthesis, Vol. 13, pp. 2055-2059.
41. **Blasco, Teresa.** *Insights into reaction mechanisms in heterogeneous catalysis revealed by in situ NMR spectroscopy.* 2010, Chem. Soc. Rev, Vol. 39, pp. 4685-4702.
42. **Yujung Dong, Maryam Ebrahimi, Aashani Tillekaratne, Juan Pablo Simonovis and Francisco Zaera.** *Hydrogenation vs. H–D isotope scrambling during the conversion of ethylene with hydrogen/deuterium catalyzed by platinum under single-collision conditions.* 2016, Phys. Chem. Chem. Phys.,, Vol. 18, pp. 19248-19258.
43. **Jilei Liu, Felicia R. Lucci, Ming Yang, Sungsik Lee, Matthew D. Marcinkowski, Andrew J. Therrien‡, Christopher T. Williams, E. Charles H. Sykes, and Maria Flytzani-Stephanopoulos.** *Tackling CO Poisoning with Single-Atom Alloy Catalysts.* 2016, J. Am. Chem. Soc., Vol. 138, pp. 6396-6399.
44. **J. Greeley, A.A. Gokhale, J. Kreuser, J.A. Dumesic, H. Topsøe, N.-Y. Topsøe, M. Mavrikakis.** *CO vibrational frequencies on methanol synthesis catalysts: a DFT study.* 2003, J. Catal. , Vol. 213, pp. 63-72.
45. **Nishiyama, H. & Inoue, Y.** *RAS study of surface acoustic wave effects on CO adsorbed on Cu surfaces.* 2005, Surf. Sci., Vol. 594, pp. 156-162.

46. **Ferri, D., Bürgi, T. & Baiker, A.** *Pt and Pt/Al2O3 thin films for investigation of catalytic solid-liquid interfaces by ATR-IR spectroscopy: CO adsorption, H2-induced reconstruction and surface-enhanged absorption.* 2001, J. Phys. Chem. B, Vol. 105, pp. 3187-3195.
47. **Chandler, B.** *DRIFTS studies of carbon monoxide coverage on highly dispersed bimetallic Pt-Cu and Pt-Au catalysts.* 2001, Catal. Today, Vol. 65, pp. 39-50.
48. **G. R. Castro, G. Doyen.** *Electronical and structural effects in CO chemisorption on $Cu_3Pt(111)$.* 1994, Surface Science, Vol. 20, pp. 384-389.
49. **Surapas Sitthisa, Trung Pham, Teerawit Prasomsri, Tawan Sooknoi, Richard G. Mallinson, Daniel E. Resasco.** *Conversion of furfural and 2-methylpentanal on Pd/SiO2 and Pd–Cu/SiO2 catalysts.* 2011, Journal of catalysis, Vol. 280, pp. 17-27.
50. **A. B. Hungria, A. Iglesis-Juez, A. Martinez-Arias, M. Fernandez-Garcia, J. A. Anderson, J. C. Conesa, and J. Soria.** *Effects of Copper on the Catalytic Properties of Bimetallic Pd–Cu/(Ce,Zr)Ox/Al_2O_3 and Pd–Cu/(Ce,Zr)Ox Catalysts for CO and NO elimination.* 2002, Journal of Catalysis, Vol. 206, pp. 281-294.
51. **E. Groppo, S. Bertarione, F. Rotunno, G. Agostini, D. Scarano, R. Pellegrini, G. Leofanti, A. Zecchina, and C. Lamberti.** *Role of the Support in Determining the Vibrational Properties of Carbonyls Formed on Pd Supported on SiO2-Al2O3,Al2O3, and MgO.* 2007, J. Phys. Chem. C, Vol. 111, pp. 7021-7028.
52. **M. L. Ang, J. T. Miller, Y. Cui, L. Mo and S. Kawi.** *Bimetallic Ni–Cu alloy nanoparticles supported on silica for the water-gas shift reaction: activating surface hydroxyls via enhanced CO adsorption.* 2016, Catal. Sci. Technol., Vol. 6, pp. 3394-3409.
53. **Min Kang, Min Woo Song, Tae Won Kim and Kyung Lim Kim.** *y-Alumina Supported Cu-Ni Bimetallic Catalysts: Characterization and Selective Hydrogenatio nof 1,3-Butadiene.* 2002, The Canadian Journal of Chemical Engineering, Vol. 80, pp. 63-70.
54. **Lavalley, J. P. Gallas and J. C.** *Comparative Study of the Surface Hydroxyl Groups of Fumed and Precipitated Silicas. 4. Infrared Study of Dehydroxylation by Thermal Treatments.* 1991, Langmuir, Vol. 7, pp. 1235-1240.
55. **Dijana Jelic, Biljana Tomic-Tucakovic, Slavko Mentus.** *A kinetic study of copper(II) oxide powder reduction with hydrogen, based on thermogravimetry.* 2011, Thermochimica Acta, Vol. 521, pp. 211-217.
56. **S.H. Park, M.S. Tzou, W.M.H. Sachtler.** *Temperature programmed reduction and re-oxidation of platinum in y-zeolites.* 1986, Applied catalysis, Vol. 24, pp. 85-98.
57. **Sofia A. Khromova, Andrey A. Smirnov, Olga A. Bulavchenko, Andrey A. Saraev,Vasiliy V. Kaichev, Sergey I. Reshetnikov, Vadim A. Yakovlev.** *Anisole hydrodeoxygenation over Ni–Cu bimetallic catalysts: The effect of Ni/Cu ratio on selectivity.* 2014, Applied Catalysis A: General j, Vol. 470, pp. 261-270.
58. **Matthew D. Marcinkowski, Matthew T. Darby, Jilei Liu, Joshua M. Wimble, Felicia R. Lucci, Sungsik Lee, Angelos Michaelides, Maria Flytzani-Stephanopoulos, Michail Stamatakis, E. Charles H. Sykes.** *PtCu Single Atom Alloys as a Coke Resistant Strategy for Efficient C-H Activation.* 2017, Manuscript submitted.

59. **Deng, W. & Flytzani-Stephanopoulos, M.** *On the Issue of the Deactivation of Au–Ceria and Pt–Ceria Water–Gas Shift Catalysts in Practical Fuel-Cell Applications.* 2006, Angew. Chemie, Vol. 118, pp. 2343-2347.
60. **Xinrui Cao, Yongfei Ji, and Yi Luo.** *Dehydrogenation of Propane to Propylene by a Pd/Cu Single-Atom Catalyst: Insight from First-Principles Calculations.* 2014, Journal of physical chemistry, Vol. 119, pp. 1016-1023.
61. **Shijun Yuan, Lijuan Meng, and Jinlan Wang.** *Greatly Improved Methane Dehydrogenation via Ni Adsorbed Cu(100) Surface.* 2013, J. Phys. Chem. C, Vol. 117, pp. 14796-14803.
62. **W. Zhang, P. Wu, Z. Li and J. Yang.** *First-Principles Thermodynamics of Graphene Growth on Cu Surfaces.* 2011, J. Phys. Chem. C, Vol. 115, pp. 17782-17787.
63. **Pao, G. Gajewski and C.-W.** *Ab initio calculations of the reaction pathways for methane decomposition over the Cu (111) surface.* 2011, J. Chem. Phys. 135, 064707
64. **N. M. Galea, D. Knapp and T. Ziegler.** *Density functional theory studies of methane dissociation on anode catalysts in solid-oxide fuel cells: Suggestions for coke reduction.* 2007, J. Catal., Vol. 247, pp. 20-33
65. **J. Li, E. Croiset and L. Ricardez-Sandoval.** *Methane dissociation on Ni (100), Ni (111), and Ni (553): A comparative density functional theory study.* 2012, J. Mol. Catal. A: Chem., Vol. 365, pp. 103-114.
66. **H. Liu, R. Yan, R. Zhang, B. Wang and K. Xie.** *A DFT theoretical study of CH4 dissociation on gold-alloyed Ni(111) surface.* 2011, J. Nat. Gas Chem, Vol. 20, pp. 611-617.
67. **Z. Jiang, L. Li, J. Xu and T. Fang**. *Density functional periodic study of the dehydrogenation of methane on Pd (111) surface.* 2013, Appl. Surf. Sci., Vol. 286, pp. 115-120.
68. **Q. Qi, X. Wang, L. Chen and B. Li.** *Methane dissociation on Pt(1 1 1), Ir(1 1 1) and PtIr(1 1 1) surface: A density functional theory study.* 2013, Appl. Surf. Sci., Vol. 284, pp. 784-791.
69. **F. Vines, Y. Lykhach, T. Staudt, M. P. A. Lorenz, C. Papp,H.-P. Steinruck, J. Libuda, K. M. Neyman and A. Gorling.** *Methane Activation by Platinum: Critical Role of Edge and Corner Sites of Metal Nanoparticles.* 2010, Chem.–Eur. J., Vol. 16, pp. 6530-6539.
70. **Simon F. J. Hackett, Rik M. Brydson Prof., Mhairi H. Gass Dr., Ian Harvey Dr., Andrew D. Newman, Karen Wilson Dr., Adam F. Lee Dr.** *High-Activity, Single-Site Mesoporous Pd/Al2O3 Catalysts for Selective Aerobic Oxidation of Allylic Alcohols.* 2007, Angewandte Chemie, Vol. 46, pp. 8593-8596.
71. **Xin Zhang, Hui Shi, Bo-Qing Xu Prof.** *Catalysis by Gold: Isolated Surface Au^{3+} Ions are Active Sites for Selective Hydrogenation of 1,3-Butadiene over Au/ZrO_2 Catalysts*. 2005, Angewandte Chemie, Vol. 44, pp. 7132-7135.
72. **Botao Qiao, Aiqin Wang, Xiaofeng Yang, Lawrence F. Allard, Zheng Jiang, Yitao Cui, Jingyue Liu, Jun Li, Tao Zhang.** *Single-atom catalysis of CO oxidation using Pt1/FeOx.* 2011, Nature Chemistry, Vol. 3, pp. 634-641.
73. **Notheisz, Gerard V. Smith and Ferenc.** *Heterogeneous Catalysis in Organic Chemistry.* s.l. : Academic Press, 1999. 978-0-12-651645-6.
74. **Songbo He, Chenglin Suna, Xu Yang, Bin Wang, Xihai Dai, Ziwu Bai.** *Characterization of coke deposited on spent catalysts for long-chain-paraffin dehydrogenation.* 3, 2010, Chemical Engineering Journal, Vol. 163, pp. 389-394.

75. **L. Vitos, A.V. Ruban, H.L. Skriver, J. Kollar.** *The surface energy of metals.* 1998, Surface Science, Vol. 411, pp. 186-202.
76. **J. Nerlov, S. Sckerl, J. Wambach, I. Chorkendorff.** *Methanol synthesis from CO_2, CO and H_2 over Cu(100) and Cu(100) modified by Ni and Co.* 2000, Applied Catalysis A: General, Vol. 191, pp. 97-109.
77. **Sean T. Hunt, Maria Milina, Ana C. Alba-Rubio, Christopher H. Hendon, James A. Dumesic, Yuriy Román-Leshkov.** *Self-assembly of noble metal monolayers on transition metal carbide nanoparticle catalysts.* 6288, 2016, Science, Vol. 352.